Eindhoven University of Technology

MASTER

Aspects of active tracking in MRI

Aben, M.J.H.

Award date:
2006

TU/e technische universiteit eindhoven

Faculty of Electrical Engineering
Division Telecommunication Technology and Electromagnetics
Chair of Electromagnetics

Aspects of active tracking in MRI

by M.J.H. Aben

EM-7-04

June, 2004

Report of Master's project performed at
TU/e, Electromagnetics Section and
The Image Science Institute, Utrecht

Supervisor:
Ir. H.J. Visser
Dr.ir. L.W. Bartels

Abstract

Active tracking antennas may be used to manoeuvre guidewires and catheters through blood vessels. The antenna detects a part of the transmitted field, allowing for the antenna to be visualised on the Magnetic Resonance Imaging (MRI) screen. A new type of antenna has been designed for tracking purposes. The new antenna has an improved sensitivity pattern, which facilitates active tracking. To compare the antenna with existing active catheter tracking coils, the sensitivity pattern of the antennas has been computed. The new antenna and the already existing antennas have been tested in vitro. From these simulations and experiments, it has been concluded that the designed antenna is suitable for active catheter tracking.

When an active tracking antenna, wire fed, or any other electrical conducting wire, is placed in an MRI scanner, the wires and the surrounding tissue may heat up. This heating is caused by the dissipation of the energy carried by the radio frequency pulse. To gain a better understanding of this phenomenon, two first-order models have been developed, that describe two measure set-ups. The data acquired from an actual measurement set-up is expected to lie in the range defined by the two extremes. In the extreme models the walls of the MRI scanner are considered to be either absent or perfectly conducting. These models have been simulated and scale models have been constructed for experimental verification. In the experiments with the scale models also a situation in between the two extremes has been constructed. From these experiments, it can be concluded that the two models are indeed extremes and that thus practical situations may be expected to yield results in between the results obtained from these two first-order models, which happen to define a relatively small solution space.

Contents

Chapter 1

Introduction

Clinical Magnetic Resonance Imaging (MRI) has traditionally been used exclusively in a role for patient diagnosis. Diagnosis and also therapy/intervention will occur as the demand for minimally invasive procedures increases. MRI systems can now provide high quality near-real-time images that facilitate a variety of image-guided procedures, many based around delivery of therapy via catheters.

1.1 Outline of the thesis

The research described in this Master's thesis is performed within the context of the "Interventional MRI (iMR)" project of the MR physics group of the Image Sciences Institute at the University Medical Centrum of Utrecht, The Netherlands. The goal of the iMR project is to make MRI suitable for the planning, guiding and evaluation of several forms of endovascular local therapy. Examples: percutaneous transluminal angioplasty, local supply of therapeutics or the placement of endovascular implants as stents. One of the main conditions that has to be fulfilled for iMR in the vasculature is that the location of the necessary instruments as catheters and guidewires can be visualised properly and reproducible with regard to the vascular anatomy.

For this visualisation, several tracking methods were proposed in the literature. One of these methods is active tracking. In active tracking micro coils are attached to the instruments which are used to measure their position. For that purpose frequency coding in three orthogonal directions is used, the position of the micro coils can be derived from the frequency of the measured MRI signal. The obtained position can be visualised (mostly by a cross) on every desired MRI image.

At the UMC, during this thesis work, expertise with active tracking has been initiated. Therefore, several aspects of active tracking have been regarded, for this Master's thesis. These aspects are: the design of the micro coils, the orientation dependence of the coil, the accuracy of the determination of the position of the micro coils and safety aspects of active catheter tracking.

Experience with active tracking has been gained mainly by making use of the Philips Electronics N.V. software and hardware package for the MRI scanner for active catheter tracking, including a catheter with a micro coil attached to it. This catheter has been made in cooperation with Cordis Corporation. This coil has a solenoidal configuration.

In chapter 2 the basic principles of an MRI scanner are explained. In the third chapter,

catheter tracking is discussed. The different techniques of active catheter tracking are shortly described. The requirements for active catheter tracking are given. With these requirements, a coil for active tracking was designed. Then the sensitivity pattern of the designed configuration was simulated and this sensitivity pattern was compared to the simulated sensitivity pattern solenoid coil made by Cordis. Then the designed configuration and the solenoid are tested in vitro, the results of these experiments are compared and discussed.

In the following chapter (4), the safety aspects of active catheter tracking are discussed. The heating problem due to induced RF energy, occur because the catheter wire gets into resonance. The resonance of a wire in an MRI scanner was modelled in two extreme situations in order to develop a first order model. These two models were simulated. In a test set up experiments with the two models were performed. These experiments were compared with the results of the simulations.

Chapter 5 gives the recommendations for further research on active catheter tracking and finally in chapter 6 this project is summarised and discussed.

Chapter 2

Magnetic Resonance Imaging

In this chapter some basic principles of MRI are discussed. This chapter only describes some aspects that are involved in active tracking. First physical aspects are discussed and then the hardware that is used by active tracking is discussed.

2.1 Physics of the nuclei

Magnetic resonance imaging (MRI) is based upon nuclear magnetic resonance. The core of an atom, the nucleus, is a collection of positively charged particles, protons, and neutral particles, neutrons. Nuclei with an odd atomic mass number, the sum of the number of protons and neutrons, or an odd atomic number, the number of protons, have a characteristic spin quantum number.
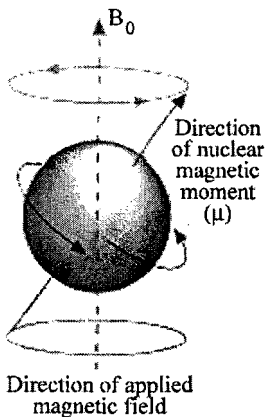
Figure 2.1: *Precession of a spinning nucleus around the axis of an applied magnetic field.*

The nucleus has mass, thus the rotation generates an angular momentum and because of the charge of the nucleus, the rotation of the nucleus induces a magnetic field with an axis parallel to the axis of spin. The magnitude and direction of the induced field is represented by the magnetic moment μ, see figure 2.1.

Normally the magnetic moments of the nuclei will be randomly oriented. When a static field, B_0, is applied, the nuclei will adopt a position in which the induced field of the nuclei align parallel to or antiparallel to the applied field. The orientation corresponds to quantum mechanical energy states [27].

2.2 Larmor precession

In the presence of the applied field, the spin vectors of the nuclei experience a torque which causes the spin vector to rotate around the axis of the applied field with a precise frequency. This cone-shaped rotation, see figure 2.1, is called Larmor precession. The rate of precession is dependent upon the physical characteristics of the isotope (atoms with the same atomic number but with different numbers of neutrons) involved and the strength of the applied magnetic field [27]:

$$\omega = \gamma B_0 \tag{2.1}$$

5

where ω the Larmor frequency in MHz, γ is a constant of proportionality, the gyromagnetic ratio, which is specific to the nucleus involved, and $\mathbf{B}_0$ is the magnetic field strength measured in Tesla. Larmor precession is a resonance phenomenon. If a system has a natural resonance, energy can be transferred to the system at this frequency very efficiently.

When the nuclei align along the $\mathbf{B}_0$ field, the magnetisation vector is in its equilibrium. In this situation no current can be induced in the receiver coils because the rotation of the nuclei is synchronic. In order to obtain information from the spins, the nuclei must be excited. The excitation is performed by irradiating the spin system with a Radio Frequency (RF) pulse at the Larmor frequency of the involved nuclei. The RF pulse induces a time dependent deflection of the magnetisation ($\mathbf{B}_1$), trough the RF coils. After the pulse, the rotation of the nuclei is synchronic, the magnetisation is precessing around $\mathbf{B}_0$ at the Larmor frequency.

Each nucleus has its own spin with its magnetic moment. The individual magnetic moments of the nuclei add up to a macroscopic magnetic moment ($\mathbf{M}$). In the absence of an applied magnetic field, the individual precessing magnetic moments are randomly oriented due to motions produced by thermal energy, thus $\mathbf{M}$ is zero. $\mathbf{M}$ can be composed of two perpendicular vector components. M_z is the component in the longitudinal plane and M_{xy} is the component in the transverse plane in a common Cartesian coordinate system as shown 2.2. To simplify the description of this motion, a rotating coordinate system is used. The
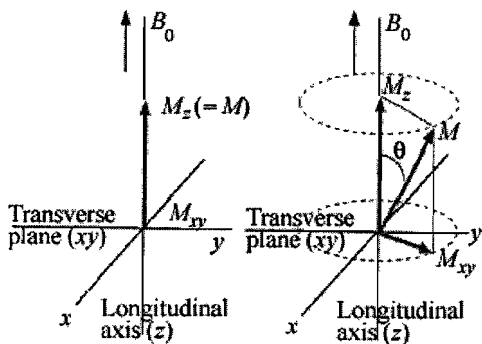
Figure 2.2: *The two components of the net magnetisation, M_z in the longitudinal direction and M_{xy} in the transverse plane. In equilibrium the net magnetisation aligns with the z-axis, only M_z contributes to the magnetisation (left). After excitation with a smal flip angle θ, the transverse component of the magnetisation, M_{xy} has become non-zero(right).*
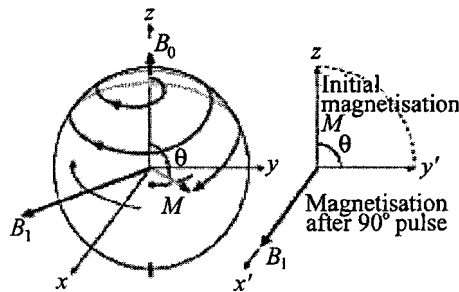
Figure 2.3: *Precession of magnetisation of a stationary magnetic field B_0 and an oscillating field B_1 during a 90° pulse, in the laboratory system (left) and in the rotating system (right).*

system rotates with the Larmor frequency around $\mathbf{B}_0$. In this rotating frame the RF pulse is represented by a additional magnetic field $\mathbf{B}_1$, perpendicular to $\mathbf{B}_0$ and that is switched on for a short period of time. The effect of $\mathbf{B}_1$ is that the magnetisation precesses about this second field and rotates away from the vertical direction toward the xy plane, as represented in figure 2.3.

The angle of rotation about $\mathbf{B}_1$, θ, is represented by [27]:

$$\theta = \gamma \int_0^\tau \mathbf{B}_1 dt \qquad (2.2)$$

6

where (2.2) B_1 is the amplitude of the RF pulse, γ is the gyromagnetic ratio, τ is the duration of th RF pulse and dt is an infinitesimal time span. θ is also called RF flip angle or RF pulse angle.

2.3 Signal detection

The detection of the MR signal is based on Faraday's law of induction:

$$V_{emf} = -N\frac{d\Phi}{dt} \qquad (2.3)$$

where N is the number of turns of the receiver coil and Φ is the flux through each turn of the receiver coil and V_{emf} is the induced voltage. Φ is defined as:

$$\Phi = \int_{coil\ area} \mathbf{B} \cdot d\mathbf{S} \qquad (2.4)$$

where $d\mathbf{S}$ the differential normal area. Faraday's law says that the induced voltage (V_{emf}) in a closed circuit is equal to the time rate of change of the magnetic flux. This principle is shown in figure 2.4. V_{emf} can be calculated from Faraday's Law.
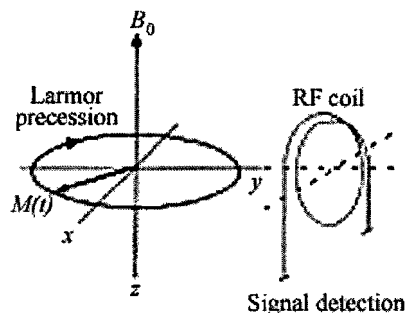
Figure 2.4: *Signal detection. The dynamic magnetic field in the xy-plane induces a voltage in the RF coil.*

2.4 Relaxation

After the excitation pulse has passed, M_z and M_{xy} return to their equilibrium. The nuclei emit electromagnetic radiation and transfer energy to the lattice or to themselves in the process of return to their equilibrium state.

The relaxation processes that influence the M_z and the M_{xy} magnetisation are independent of one another, see figure 2.5. In general M_{xy} will have disappeared before M_z is fully restored. Both relaxation processes hebave exponentionally.

2.4.1 T_1 - relaxation

T_1- relaxation is also called longitudinal relaxation. It occurs by spin-lattice interaction. Following termination of the RF pulse, the nuclei will transfer a part of their their energy as heat to the lattice and revert to their equilibrium position. Realignment of the nuclei along B_0 leads to a gradual increase of M_z. This process of equilibrium restoration following a $\theta = 90°$ RF pulse at $t = 0$, is described by the following equation [27]:

$$M_z = M_0 \cdot \left(1 - e^{-t/T_1}\right) \qquad (2.5)$$

where M_0 is the amount of magnetisation parallel with B_0 before an RF pulse is applied and T_1 is the time required for the M_z to return to 63% of its original value. T_1 - relaxation is shown in figure 2.5.

Figure 2.5: *The longitudinal and transverse magnetisation during relaxation. T_1 is the time required for the longitudinal magnetisation to return to 63% of its original value. T_2 is the time required for the transverse magnetisation to fall 37% of its original value.*
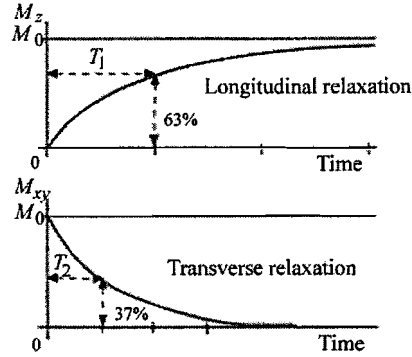
The efficiency of energy transport between spins and lattice determines T_1. This depends on molecular motion and the structure and physical state of the tissue. T_1 is higher in solids and pure liquids.

T_1 relaxation times in biological tissue range from a few milliseconds to a few seconds. T_1 relaxation times depend on $\mathbf{B_0}$

2.4.2 T_2 - relaxation

T_2- relaxation is also called transverse relaxation. It occurs by spin-spin interaction. Spin-spin interaction causes dephasing. After the RF pulse is excited, the spins of the nuclei are in phase. Interactions between individual spins create local magnetic field variations that cause fluctuations in the precessional frequency of the individual nuclei. This results in a gradual and random dephasing of the spins, which causes a decay in the magnitude of M_{xy}. This process of equilibrium restoration following a $\theta = 90°$ RF pulse at $t = 0$, is described by the following equation [27]:

$$M_{xy} = M_0 \cdot e^{-t/T_2} \tag{2.6}$$

where M_0 is the amount of transverse magnetisation before an RF pulse is applied and T_2 is the time required for M_{xy} to fall by 63% of its original value. T_2 - relaxation is shown in figure 2.6.

The efficiency of energy transport between spins determines T_2. This depends on the structure and physical state of the tissue, solids and large molecules have a short T_2, small molecules have a long T_2. The presence of macromolecules in solution shortens T_2. T_2 is independent of the field strength.

Figure 2.6: *Difference between T_2^* and the T_2.*

T_2 relaxation times in biological tissue range from a few milliseconds to a few seconds. Inhomogeneities in the applied field also contribute to the dephasing process, spin coherence is also affected by them. The exponential decay in
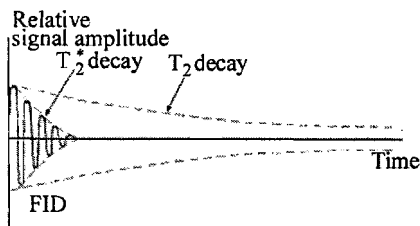
8

signal resulting from the combination of T_2 relaxation and field inhomogeneities is referred to as T_2^*, the effective transverse relaxation time. This is shown in figure 2.6.

2.5 Gradients

For active tracking only the part of the body/phantom in which the catheter is situated has to be scanned. This done by applying field gradients.

MRI uses magnetic field gradients to create spatial differentiation of the signals emitted from the region of interest in a patient. The magnetic field gradient is a weak magnetic field that changes linearly with position and is superimposed on the main magnetic field, in three orthogonal directions. All gradient magnetic fields point in the $\mathbf{B_0}$ direction. Gradient fields yield a position-dependent Larmor frequency. For example, the equation for the Larmor frequency in the x direction becomes [27]:

$$\omega = \gamma \cdot (B_0 + G_x \cdot x) \tag{2.7}$$

where G_x is the applied constant gradient field in the x direction and x is the distance in the x direction in meter.

Every transverse slice in the patient resonates at a different Larmor frequency when a gradient field is applied. The slice thickness and location of slice are determined by the bandwidth of the RF pulse and gradient in direction of slice selection. This is shown in figure 2.7. For active tracking gradient fields are applied in three directions, three orthogonal readouts are obtained from which the position of the catheter can be determined in three dimensions.
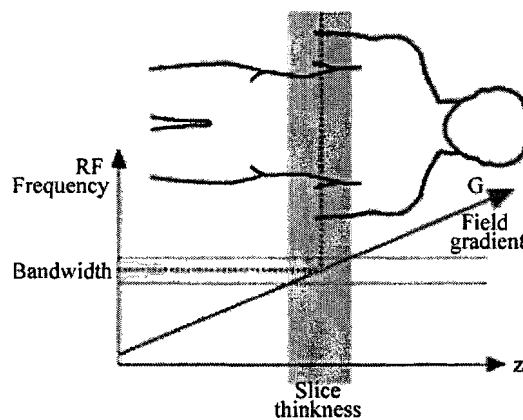

Figure 2.7: *Magnetic field gradient to perform slice selective excitation.*

2.6 MRI hardware

In this section a short summary is given of the main hardware components of a basic MRI scanner, see figure 2.8.

RF Shielded Room

| Magnet |
| Gradient Coils |
| RF Coil |

Patient

| RF Coil |
| Gradient Coils |
| Magnet |

| Gradient Amplifier | RF Amplifier | RF Receiver |
| Gradient Pulse | RF Pulse | AD Converter |

Computer
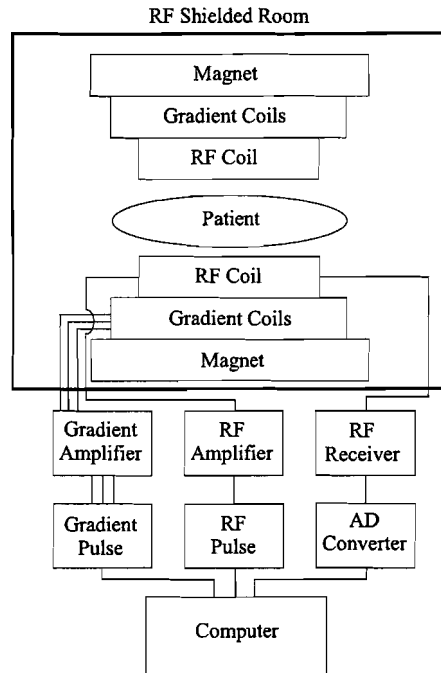
Figure 2.8: *Block diagram of an* MRI *system [19]*

Superconducting magnets are able to generate strong fields. Once started the current will flow in the coils indefinitely, provided that the temperature is kept below the critical temperature by cooling with liquid helium. The fields from such magnets are very stable with time, which is essential for an MRI system. These magnets are used to generate the static $\mathbf{B}_0$ field.

The gradient coils, gradient amplifier and gradient pulse are used for spatial selection and encoding. When three gradient coils are used, three orthogonal readouts are available and the position of the catheter can be determined in three dimensions.

The third main component of an MRI scanner are the RF coils. The RF pulses are applied through an RF generation system, consisting of a transmitter and an RF coil. The RF transmit coil excites nuclei with the energy generated by the transmitter. The RF receive coil detects the re-emitted signal from the nuclei.

Amplifiers and the AD converter reduce noise, demodulate the signal and transport it to a computer system for reconstruction. The RF shielding protects the system from external RF interferences and protects everything outside the room from the $\mathbf{B}$ fields in the room [19].

Chapter 3

Catheter tracking

MRI has traditionally been used for patient diagnosis. Due to recent improvement in technical specifications, MRI is evolving into a tool for guidance and evaluation of minimally invasive therapeutic interventions. This is called interventional magnetic resonance imaging (iMRI). Catheter tracking is part of iMRI. In Duerk et al. [10] a summary on catheter tracking can be found. Three methods of catheter tracking are described: active catheter tracking, passive catheter tracking and semi-active catheter tracking. These three methods are not sharply defined. For this reason Bartels et al. [6] proposed a new classification into global and local detection. Global detection refers to strategies in which some kind of signal alteration in MR images provoked by the instruments is used for detection of the location of the endovascular devices [6]. With local detection, only the proton resonance signal arising from spins in the direct vicinity of the instruments is detected by using the instrument itself as the receive antenna [6]. These strategies are shortly described below.

Device tracking using global detection

Several visualisation and tracking approaches have been proposed that are based on the principle of global detection. The instruments that are used with these techniques can be divided into two groups:

- Instruments, not connected to external hardware, providing disturbances that cannot be switched off, these will be referred to as non-switchable [6].
- Instruments, either electrically or optically connected to external hardware, that can be switched off, these will be referred to as switchable [6].

In this section examples of these two groups of devises are given.

Non switchable devisees

An example of a non-switchable device is the susceptibility-based tracking catheter proposed by Bakker et al. [3] proposed. Bakker et al. attached small ringmarkers on a catheter. These ringmarkers were made of strongly paramagnetic dysprosium oxide. They are consistent visualised, regardless of the angulation of the device with respect to the main magnetic field.

Switchable devisees

An example of switchable devices are the coils made by Glowinski et al [13, 14]. A thin wire loop is incorporated in the wall of the used catheter. This wire is used to induce a local

magnetic field that disturbs the homogeneity of the main magnetic field of the MR scanner. The local fields are established by injecting a small current trough the wire. This results in signal loss in the vicinity of the device due to dephasing, described in section 2.4 and this leads to a disturbance of the phase image [13, 14]. The severity of the artifacts can be adjusted by adjusting the current through the wire.
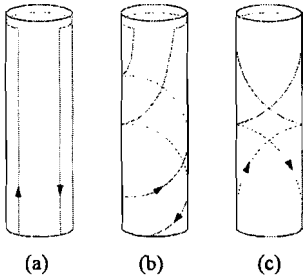

Figure 3.1: *The different wire configurations Glowinski et al. [14] regarded. Straight antiparallel (a), double helix (b) and opposed double helix (c).*

Glowinski et al. [14] looked at several wire configurations for the catheter. The considered configurations are shown in figure 3.1. The catheter should be independent of the wire configurations orientation, it should be visual at all orientations. Glowinski showed that the catheter with the straight antiparallel wire, figure 3.1(a), is orientation dependent. The other configurations are less sensitive of the orientation because of a changing wire direction along the shaft. The opposed double helix configuration, figure 3.1(c), gave the best results. The distance between the two wires in a cross section of the catheter varies. This results in a typical well detectable inhomogeneous pattern along the catheter. As the directions of the wires change, at least one fraction of the wires always has components along $\mathbf{B}_0$.

Another example of a switchable device: Wong et al. [38] used a method that involves the integration of a photoresistor in a intravascular MRI receiver coil. A fiberoptic cable extending the length of the interventional device is used in conjunction with an external light source to deliver light to the photoresistor. Exposing the photoresistor to light changes its bulk resistance and greatly lowers the quality factor of the parallel resonant circuit, effectively detuning it. By combining the optical detuning scheme with inductive coupling of the interventional device-mounted micro coils to a standard MRI coil, a completely wireless device for active device tracking has been created. The system is shown in figure 3.2
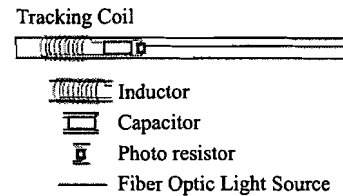
Figure 3.2: *Schematic of component layout for a single coil active tracking system [38].*

Device tracking using local detection

In device tracking using local detection, the instrument itself is operating as a receive antenna connected to the receiver channel of the scanner. The instruments are said to be actively visualised. An example device tracking using local detection of is described below.

Active tip tracking

Active tip tracking, further referred to as active tracking, is an example of device tracking using global detection. The locating of the tip is performed by equipping the catheter with one or more small receiver coils at the tip with electric leads connected to the MR receiver.

The localised spatial sensitivity of the small coils leads to a peak in the detected MR signal. The location of the peak in the frequency spectrum directly transforms to the location of the coil along that axis [11, 23]. By applying spatial frequency encoding in three orthogonal directions, the receiver coil at the tip of the catheter can be located in three dimensions by the used of three perpendicular gradients, section 2.5. This location is projected on a previously acquired road map image. Since the three dimensional position of the cluster of coils is known, its position can be projected onto multiple images in multiple planes, therefore biplanar or triplanar tracking is possible.

A single one-element micro coil incorporated into an interventional device can only supply tip position information. Coils on multiple positions on the device are necessary for being able to also determine its orientation. For orientation information, multiple coils have to be used [41] or, like in Zhang et al. [40], a single micro coil with three separate winding elements may be used that provides both the device orientation and tip position.

Zhang et al. [40] made a micro coil design with three separate winding elements that provide both the tip position and the device orientation. When a multi element coil is used for signal detection and a field gradient is applied, multiple peaks will be found that correspond to the locations of the multiple winding elements of the coil. The elements are placed unequally, as shown in figure 3.3. This is done to create unique correspondence between the peak and the winding elements.
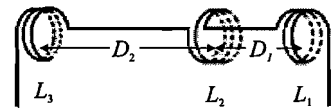

Figure 3.3: *The single coil design with unequally spaced elements ($D_2 > D_1$) designed by Zhang et al.*

An advantage of this methods is that if micro coils (very small) are used, the flexibility of the catheter will hardly be affected. A disadvantage is that only the position of a single point is visualised and the orientation of the catheter remains undetermined. Another drawback is that active tracking needs additional hardware and software connected to the MRI scanner. Also the heating due to induced RF energy is a drawback of this method.

An advantage of using more than one coil is that the orientation of the catheter is also determined. A disadvantage is that the bending of the catheter is limited by the length of the multi element coil.

3.1 Active catheter tracking

The assignment of this thesis was to develop an antenna for active catheter tracking, therefore only active catheter tracking is discussed in this report. For active tracking purposes one or more coils have to be attached to the inserted instrument. These coils have to satisfy several conditions, these are described in the first subsection. As said before, active tracking needs additional hardware connected to the MRI scanner, the hardware and software used in this thesis is described in the following subsection.

3.1.1 Antenna specifications

An antenna that is used for active tracking has to meet the following conditions:
- Local sensitivity
- High sensitivity
- Orientation independent

13

The the antenna has to be well detectable. This means that the sensitivity pattern of the antenna has to show a localised and high peak. Furthermore the sensitivity pattern has to be insensitive to the coil orientation, it has to show a localised and high peak at any orientation.

The coil has to be small and flexible. The coil is attached to the catheter or guidewire that has to remain flexible to manoeuvre through the vessels. Because of that reason the coil also has to have a small diameter and length. If only one coil is used in the catheter, the orientation of the coil remains unknown. To solve this, multiple coils can be included. From the so created multiple peaks in the sensitivity pattern the orientation of the catheter can be obtained.

For clinical active catheter tracking, the catheter and system have to be inherently safe [26]. Describing this report, the devices are not safe because of the conducting wires. The wires may be heated by the induced RF energy. In Chapter 4 the safety aspects of active tracking are discussed. This is at the moment not considered a problem since the designed coils are only used in laboratory settings.

3.1.2   Additional hardware and software

For active tracking, additional hard and software is necessary. For this project a Philips Electronics N.V package is used.

The hardware consists of a "Catheter Preamp Box", which is used for tuning and preamplification of the micro coil signal, and a "Catheter Interface Box", which is used for the connection of the micro coil signal to the MRI scanner and to supply the power and the detuning signal for the "Catheter Preamp Box". The active catheter has to be attached to the "Catheter Preamp Box" for amplification of the received MR signal as well as for tuning and matching of the micro coil that is on the tip of the catheter [34]. The "Catheter Interface Box" is connected to the MRI scanner via the synergy coil connector, see figure 3.5 The synergy coil is attached to the MRI scanner via the "Catheter Interface Box". The synergy coil is used for acquiring the MRI images on which the position of the catheter is depicted.

Figure 3.4: *Coil made by Cordis. The coil has a height H and a radius r.*

The software detects the micro coil within the imaging plane and displays a cross where the coil is localised on the last acquired roadmap image [32].

Cordis Corporation developed various versions of active tracking catheters for the hardware and software developed by Philips. Cordis produces devices for minimal invasive procedures, like catheters. The catheters are based on 5F double lumen catheter tube. The micro coil is wound onto the tip as a 15 turns solenoid, figure 3.4, with 0.28 pitch made from insulated 0.08 *mm* copper wire.

Due to restrictions of the used hardware and software only a coil that provides one peak can be used. The software detects the peak in the received signal, so a coil that produces multiple peaks cannot be used. Only one coil can be connected to the hardware, so only one coil can be used. Due to these restrictions here the only the location of the tip can be obtained.
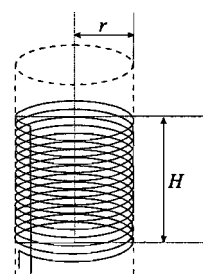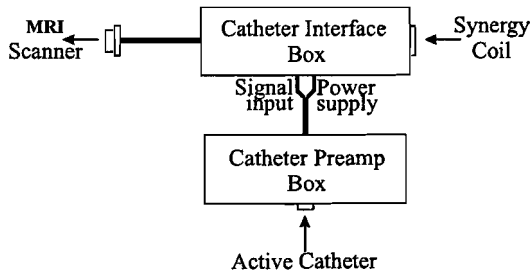
14

Figure 3.5: *Hardware connection of an active catheter to the* MRI *scanner.*

3.2 Antenna design

The coil developed by Cordis did not give very good results for active catheter tracking. The coil did not meet all requirements for active tracking. Therefore a new design for a active tracking coil had to be made that meets the requirements better.

Weiss et al. [35] developed orientation independent fiducial markers for instrument localisation. A fiducial marker provides a clear and accurate reference point. Fiducial markers are not attached to the MRI scanner by a wire. Weiss et al. described a set up of two separate resonant circuits, wherein two coils are placed into each other, see figure 3.6. Furthermore, the windings of the coils are positioned, relative to the catheter axis, under angle α, see figure 3.7. If α is $\pi/4$, the two coils are placed perpendicular with respect to each other.
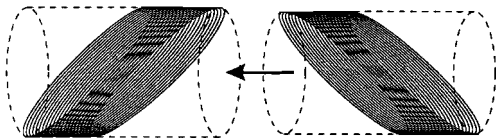

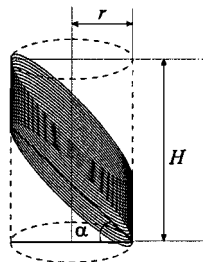Figure 3.6: *The configuration of the two coils perpendicular to each other.*

Figure 3.7: *The coil is wound α angle to the catheter axis, has a height H and a radius r.*

Kuehne et al. did in vitro and in vivo experiments with the fiducial markers described above [21]. With the in vitro experiments the fiducial markers were attached to a catheter and placed in a saline bath. The catheter was tested at different angles of rotation with respect to be B_0 field. It was found that in vitro, the fiducial marker was fast and reliably identifiable against the background at all orientations. In the in vivo experiment, the fiducial markers were attached to a catheter and introduced into the vascular system of a swine. The catheter was tested at different orientations in the vascular bloodpool. A result of the in vivo experiments was that there was a excellent signal contrast between the fiducial marker and the vascular bloodpool.

Because of the reported excellent test results, the fiducial marker were taken as a starting point for the development of an active tracking antenna. The layout of these fiducial markers is chosen as layout for the micro coils for active catheter tracking because of the orientation independence. The height H and radius r of the coils are defined as shown in figure 3.7.

Analysis of the two perpendicular coils with the 45° orientation with respect to the coil axis
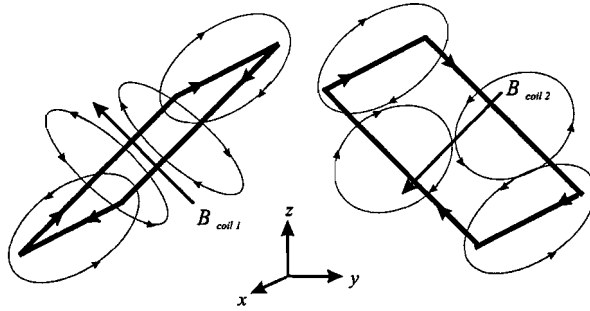

Figure 3.8: *Direction of the B field due to a current in the coils*

The sensitivity pattern of the antenna used for active tracking has to meet some requirements. The sensitivity pattern of an antenna is related to the **B** field induced by the antenna,

$$S = \frac{B}{I}$$

were **S** is the sensitivity and **I** the current flowing through the antenna. Therefore **B** field is analysed.

In figure 3.8 one winding of the left coil and one winding of the right coil from figure 3.6 are shown. For reasons of clarity the windings are represented as rectangles. The coils are assumed to be connected in series, so the current trough the coils is in the same direction, here assumed to be clockwise. With help of the righthanded screw rule [31], the direction of **B** around the line segments can be derived. Some magnetic induction field lines (circles) are shown in figure 3.8. The direction of the **B** field is also indicated. The total **B** at a specific point follows from the vectorial addition of all **B** field components in that point. In the center of the coils all field lines point in the same direction, so the **B** field is concentrated at the center of the coil. The direction of the **B** field in the center of the coil surface is perpendicular to the coil. The **B** field in the center of the coil is shown in figure 3.8 as $\mathbf{B}_{coil\ 1}$ for the left coil and $\mathbf{B}_{coil\ 2}$ for the right coil. The rectangular x, y, z coordinate system is chosen such that $\mathbf{B}_{coil\ 1}$ and $\mathbf{B}_{coil\ 2}$ lay in the yz plane.

In the antenna configuration, the two coils are placed into each other, so the two windings of figure 3.8, representing the two coils, are placed into each other, figure 3.9. The $\mathbf{B}_{coil\ 1}$ and $\mathbf{B}_{coil\ 2}$ in the center of the coils can be vectorially added, the resulting B field is represented in the figure as $\mathbf{B}_{res}$, here pointing in the y direction. When the catheter is placed in the MRI scanner in the z direction , the rotation around the x and y axis respectively is zero. $\mathbf{B}_{res}$ is perpendicular to the $\mathbf{B}_0$ field of the MR scanner, the xy plane. Signals in the xy plane can be measured by the MR scanner, because of the $\mathbf{B}_0$ field that is aligned along the z direction.

The **B** field induced by one coil cancels the **B** field of the other coil at the xz plane in the middle of the two coils, the grey area in figure 3.9. The plane extends to outside the coils. The cancellation occurs for line segments of the two different coils, in which the current flow in the same direction. For example, the line cd in figure 3.9 lies between the two lower segments of the coils. The currents of these two segments flows in the same direction. The directions of the **B** fields (circles), induced by both segments, at a evaluated point on the line

16

cd are opposite, as shown in figure 3.9. When the **B** fields are vectorially added, they cancel each other. This cancellation happens in the whole gray area.

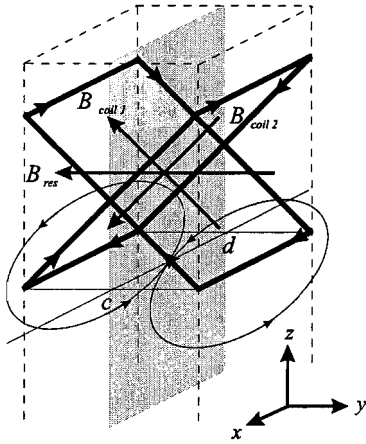Figure 3.9: *The B field of the two perpendicular coils*

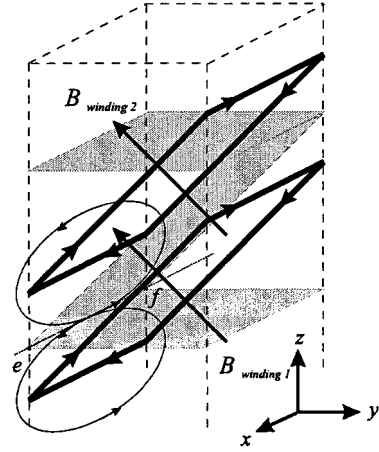Figure 3.10: *The B field of the two windings of one of the coils.*

In figure 3.10 one coil is represented by two windings. For simplicity reasons, each winding consist of four segments. At the planes between the segments of the coil, shown as the grey area in figure 3.10, the **B** fields due to those segments are also cancelled. In figure 3.10, the grey areas also extend outside the coils. For example, the line *ef* in figure 3.10 lies in the plane defined by the two lower segments of each winding having equal distance to both of these segments. The direction of the **B** fields at the line is opposite, as shown in figure 3.10, so they cancel each other. The cancellation of the **B** fields due to the parallel segments takes place at all planes positioned exactly between two similar segments of the two coils.

In the grey areas shown in figures 3.9 and 3.10 the **B** fields are are cancelled. At the center of the coils, the **B** fields of the perpendicular coils, $\mathbf{B}_{coil\ 1}$ and $\mathbf{B}_{coil\ 2}$, add in phase. The cancellation of the **B** fields as discussed contributes to the concentration of the field in the center of the coil. for active tracking a localised peak in the sensitivity pattern is desired.

The **B** field of a solenoid coil, like the one made by Cordis is also concentrated in the center of the coil, but there, only the cancellation of the **B** fields due to the phenomenon shown in figure 3.10 exists. The net **B** field of the two perpendicular coils inside each other is more localised than the **B** field of a solenoid coil. This is due to the additional cancellation of the **B** fields at certain regions of the coil compared to the solenoid.

3.3 Simulations

The sensitivity field (i.e. the **B** field) of the designed coils and the solenoid coil had to be compared, to see which one meets the requirements at best. First, Biot-Savart's Law is discussed. Biot-Savart's Law is used for the calculation of the magnetic fields due to a current in a line. To calculate the magnetic field of the coils, the coils are divided in line segments. Op den Kamp [19] verified that a static model may be used for the determination of the sensitivity pattern of intravascular MRI antennas. This law is the base for the routine used for the sensitivity pattern calculation. The simulation results of this routine are shown in this

17

section for the different coils.

3.3.1 Biot-Savart's Law

The Biot-Savart Law relates magnetic fields to the currents in lines, which are their sources. This method assumes a direct current flowing through the lines. The law states that the magnetic field intensity dH produced at a point P, as shown in figure 3.11, by the differential current element $I\,dl$ is proportional to the product $I\,dl$ and the sine of the angle α between the element and the line joining P to the element [31],
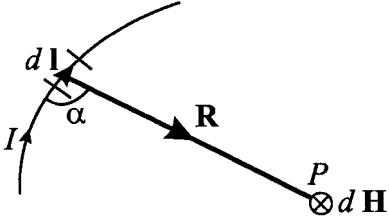
$$dH = \frac{I\,dl\,\sin(\alpha)}{4\pi R^2} \qquad (3.1)$$

Figure 3.11: *Magnetic field dH at P due to current element Idl.*

By the use of the cross product between two vectors,

$$\mathbf{A} \times \mathbf{B} = AB \sin\theta_{AB}\,\mathbf{a}_n \qquad (3.2)$$

where $A = |\mathbf{A}|$, $B = |\mathbf{B}|$, θ_{AB} is the angle between $\mathbf{A}$ and $\mathbf{B}$ and $\mathbf{a}_n$ is the normal vector on the plane defined by $\mathbf{A}$ and $\mathbf{B}$. Equation (3.1) can be rewritten in vector form,

$$d\mathbf{H} = \frac{I\,dl \times \mathbf{a}_R}{4\pi R^2} = \frac{I\,dl \times \mathbf{R}}{4\pi R^3} \qquad (3.3)$$

where $R = |\mathbf{R}|$ and $\mathbf{a}_R = \mathbf{R}/R$. For a wire carrying current I, the Biot-Savart law as in equation (3.3) becomes

$$\mathbf{H} = \int_L \frac{I\,dl \times \mathbf{R}}{4\pi R^3} \qquad (3.4)$$

where integration is on the length of the wire L. This equation can be rewritten in terms of the B-field by the use of,

$$\mathbf{B} = \mu\mathbf{H} \qquad (3.5)$$

assuming an isotropic medium and becomes

$$\mathbf{B} = \mu \int_L \frac{I\,dl \times \mathbf{R}}{4\pi R^3} \qquad (3.6)$$

The Biot-Savart law is used to calculate the magnetic field intensity of the designed coil. The coil was represented by a finite set of straight wire segments. The calculation of the magnetic field intensity involved the Biot-Savart equation for all components of the segments of the conductor that make up the coil [24].

The coil had to be parameterised in small wire segments. For each wire segment, the magnetic field was evaluated at a point (x_0, y_0, z_0) for a current flowing from a point (x_1, y_1, z_1) to another point (x_2, y_2, z_2). The magnetic fields produced by a sequence of straight line segments is the sum of the field which are calculated for each line segment. For each line segment equation (3.6) can be written as [24],

$$\mathbf{B} = \frac{\mu I}{4\pi} \left(\int \frac{D_x dt}{(A + Bt + Ct^2)^{\frac{3}{2}}}\,\hat{x} + \int \frac{D_y dt}{(A + Bt + Ct^2)^{\frac{3}{2}}}\,\hat{y} + \int \frac{D_z dt}{(A + Bt + Ct^2)^{\frac{3}{2}}}\,\hat{z} \right) \qquad (3.7)$$

18

where,

$$A = (x_1 - x_0)^2 + (y_1 - y_0)^2 + (z_1 - z_0)^2 \tag{3.8a}$$

$$B = 2\left[(x_1 - x_0)(x_2 - x_1) + (y_1 - y_0)(y_2 - y_1) + (z_1 - z_0)(z_2 - z_1)\right] \tag{3.8b}$$

$$C = (x_2 - x_1)^2 + (y_2 - y_1)^2 + (z_2 - z_1)^2 \tag{3.8c}$$

$$D_x = (y_2 - y_1)(z_1 - z_0) - (z_2 - z_1)(y_1 - y_0) \tag{3.8d}$$

$$D_y = (z_2 - z_1)(x_1 - x_0) - (x_2 - x_1)(z_1 - z_0) \tag{3.8e}$$

$$D_z = (x_2 - x_1)(y_1 - y_0) - (y_2 - y_1)(x_1 - x_0) \tag{3.8f}$$

in terms of parameter t. The parameter t was integrated from 0 to 1.

Equations (3.7) and (3.8) were used to calculate the field of the designed coils. They were implemented in a FORTRAN routine. The designed coil was divided in a number of line segments. For each of these segments the contribution of the magnetic field at a point (x_0, y_0, z_0) was calculated. The total magnetic field at point (x_0, y_0, z_0), (B_x, B_y, B_z), is the sum of the contributions to the magnetic field of all of the individual line segments.

Only the signal in the transverse plane is received. Usually the radiation pattern of an antenna is used to make a comparison with other antennas. The radiation pattern of an antenna is usually defined for free-space applications and relates to to the far-field region. For MR antennas this pattern is not suitable because the antennas will be surrounded by blood and tissue and the region of interest is the near field region [19]. Therefore the sensitivity is used here for comparison. The sensitivity pattern of an antenna expresses the sensitivity of the antenna to the magnetic field in different directions. This measure is used to compare different antennas. The sensitivity is defined as [19]

$$S = \frac{\sqrt{B_x^2 + B_y^2}}{I} \tag{3.9}$$

The unit of S is Tesla per Ampere ($\frac{T}{A}$). S only depends on the x and y component of the B field, B_x and B_y respectively because of the presence of the $\mathbf{B}_0$ in the z direction. For the orientation dependence a rotation matrix was included. The equation for the sensitivity has to be adapted to the rotation matrix,

$$S = \frac{\sqrt{B_x'^{\,2} + B_y'^{\,2}}}{I} \tag{3.10}$$

where

$$B_x' = B_x R_{xx} + B_y R_{xy} + B_z R_{xz} \tag{3.11}$$

$$B_y' = B_x R_{yx} + B_y R_{yy} + B_z R_{yz} \tag{3.12}$$

In equation (3.11) and (3.12), R_{xx} trough R_{zz} are respectively defined as [19],

$$R_{xx} = \cos\theta \cos\psi$$

$$R_{xy} = \cos\psi \sin\theta$$

$$R_{xz} = -\sin\psi$$

19

$$R_{yx} = -\cos\phi\sin\theta + \cos\theta\sin\phi\sin\psi$$
$$R_{yy} = \cos\theta\cos\phi + \sin\theta\sin\phi\sin\psi$$
$$R_{yz} = \cos\psi\sin\phi$$

$$R_{zx} = \sin\phi\sin\theta + \cos\theta\cos\phi\sin\psi$$
$$R_{zy} = -\cos\theta\sin\phi + \sin\theta\cos\phi\sin\psi$$
$$R_{zz} = \cos\psi\cos\phi$$

where ϕ, ψ and θ are the rotation angles around the x, y and z axis respectively.

3.3.2 Comparison of the coils

The sensitivity patterns of the two perpendicular coils was simulated with the FORTRAN routine. The output file of the sensitivity pattern was plotted in MATLAB. The begin and end coordinates of the different line segments, the coil is made of, were defined in the input of the FORTRAN routine. For the calculation of the sensitivity patterns, a 0.01 mA DC current was supposed to flow through the antenna, this is expected to be a realistic value [19]. The value of I does not contribute to the sensitivity pattern because of the definition of the sensitivity pattern in equations (3.9) and (3.10). The rotation angles around the x, y and z axis, ϕ, ψ and θ are supposed to be 0°.

For active tracking one or more coils have to be attached to the inserted instrument. When a catheter is inserted, first a guidewire is inserted and then the catheter is guided over the guidewire, so the active tracking coil has to be integrated into the guidewire. Eventually the coils that are designed later in this section were tested in vitro. Because it is too difficult to make a coil integrated in a guidewire by hand, a catheter is used here to place the active tracking coil on.

The solenoid coil had the following characteristics: $H = 5.0$ mm, $r = 0.8$ mm and $N_{turns} = 15$, see figure 3.13. These measurements were used because the solenoid coil made by Cordis has this size.

The single coil with the 45° orientation with respect to the coil axis had the following characteristics: $\alpha = 45°$, $H_{coil} = 3.0$ mm, $r_{coil} = 0.8$ mm and $N_{turns\ coil} = 15$, see figure 3.12. This was supposed to be the inner coil of the two perpendicular coils placed in each other.

The two perpendicular coils with the 45° orientation with respect to the coil axis of the had the following characteristics: $\alpha = 45°$ for both coils, $H_{coil1} = 3.0$ mm, $r_{coil1} = 0.8$ mm and $N_{turns\ coil1} = 15$. $H_{coil2} = 3.0$ mm, $r_{coil2} = 0.9$ mm and $N_{turns\ coil2} = 15$. α of both coils is 45°.

To make a comparison the coils with with the 45° orientation with respect to the coil axis had the same number of windings. The radius of the coils is related to the radius of the used catheter. The height of the coils is determined by the radius of the catheter and the radius of the copper wire of the coil. When 0.09 mm copper wire is used the height of the coils with the 45° orientation with respect to the coil axis becomes 3.0 mm. The used copper wire had a diameter of 0.09 mm so if the second coil is wound, the radius is approximately 0.09 mm bigger, but the coils have to be glued together, so the difference of 0.1 mm between the two radii is a realistic value.
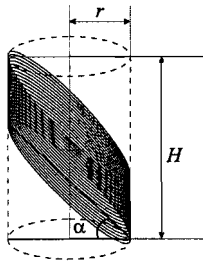
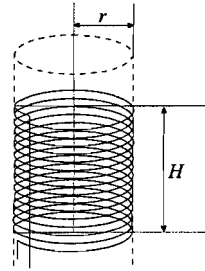Figure 3.12: *The coil is wound α angle to the catheter axis, has a height H and a radius r.*

Figure 3.13: *Coil made by Cordis. The coil has a height H and a radius r.*

Results

Single coil with the 45° orientation with respect to the coil axis

This simulation was performed since for the in vitro experiments only one of the two perpendicular coils was used. In figure 3.14 the sensitivity pattern of one of the two perpendicular coils is shown. The color scale in figure 3.14 is the amplitude of the sensitivity pattern, the unit of the color scale is $\left[\frac{T}{A} \cdot 10^{-1}\right]$.

The sensitivity patterns of one of the perpendicular coils with the 45° orientation with respect to the coil axis, figure 3.14, has a localised pattern in the xy plane, there is not much spread of the pattern outside the coils. The width of the sensitivity pattern in the xy plane is approximately 2 m, the width of the sensitivity pattern is related to the width of the catheter. Only the xy plane can be sampled with the MR scanner.

Two perpendicular coils with the 45° orientation with respect to the coil axis

In figure 3.15 the sensitivity patterns of the two perpendicular coils with the 45° orientation with respect to the coil axis is shown. The color scale in figure 3.15 is the amplitude of the sensitivity pattern, the unit of the color scale is $\left[\frac{T}{A} \cdot 10^{-1}\right]$.

For the two perpendicular coils, two coils with the 45° orientation with respect to the coil axis, were placed into each other. The radius of the outer coil was a bit larger than the radius of the inner coil, for the simulations the radius of the outer coils is taken 0.1 mm larger than the radius of the inner coil. The sensitivity pattern of the outer coil approximates the sensitivity pattern of the inner coil reflected in the z axis. Because the patterns of the inner and outer coil are highly localised and do not spread much outside the coils, the pattern of both coils combined, figure 3.15, is also highly localised in the xy plane and does not spread much outside the coils. The width of the sensitivity pattern in the xy plane is approximately 2 m, the width of the sensitivity pattern is related to the width of the catheter.

Solenoid

In figure 3.16 the sensitivity pattern of the solenoid coil is shown. The color scale in figure 3.16 is the amplitude of the sensitivity pattern, the unit of the color scale is $\left[\frac{T}{A} \cdot 10^{-1}\right]$.

The sensitivity pattern of the solenoid coil has a lower amplitude than observed in the two previous configurations and is not very localised in the xy plane. Only one winding is visible and there is no signal in the center of the coil.

Discussion and conclusions

The simulations of the sensitivity pattern of one of the coils with the 45° orientation with respect to the coil axis show a localised peak. The peak is approximately 2 mm in diameter. This is due to the radius of the used catheter, which is related to the vessel diameter in which the catheter is inserted. Catheters with a radius of 0.8 are used in large (diameter 0.5-1.5 cm) veins and arteries. The pixels of the MR imager are 1.3722 mm × 1.3722 mm. Thus the depicted cross is expected to jump between two pixels, for procedures in large vessels this is acceptable. Considering these results this coils is expected to be suitable for active tracking.

The simulations of the sensitivity pattern of the two perpendicular coils with the 45° orientation with respect to the coil axis also show a localised peak. The amplitude of the peak is higher than the peak in the sensitivity pattern of one coil with the 45° orientation with respect to the coil axis, it is a result of the addition of the two sensitivity patterns of the separate coils. Here the peak is also approximately 2 mm in diameter, so here the depicted cross is expected to jump between two pixels. Considering these results these coils are expected to be suitable for active tracking.

The simulated sensitivity pattern of the solenoid coil is not very localised, so it is harder for the software to determine the position of the coil. Therefore the coil is less suitable for active tracking.
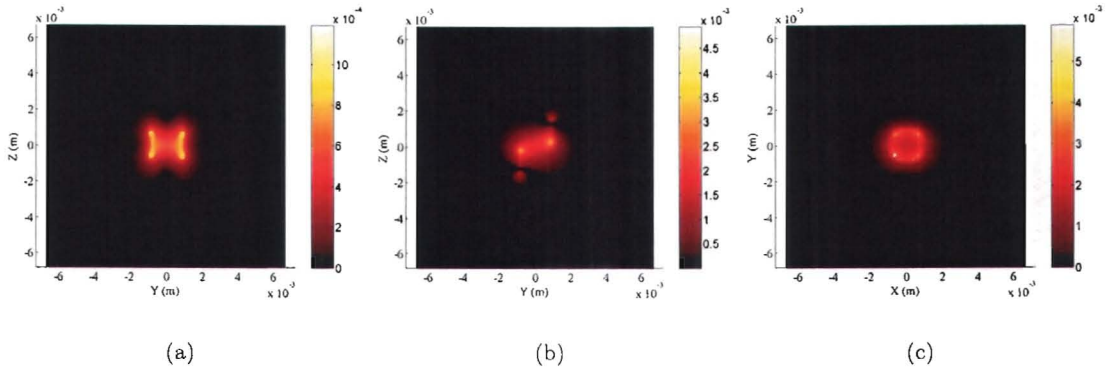
(a)   (b)   (c)

Figure 3.14: *Sensitivity pattern* $\left[\frac{T}{A} \cdot 10^{-1}\right]$ *of coil 1 in the xz plane at* $y = 0$ *(a), in the yz plane at* $x = 0$ *(b) and in the xy plane at* $z = 0$ *(c).* $\alpha = 45°$, $H_{coil} = 3.0$ *mm,* $r_{coil} = 0.8$ *mm and* $N_{turns \ coil} = 15$.

(a)   (b)   (c)

Figure 3.15: *Sensitivity pattern of* $\left[\frac{T}{A} \cdot 10^{-1}\right]$ *the two perpendicular coils in the xz plane at* $y = 0$ *(a), in the yz plane at* $x = 0$ *(b) and in the xy plane at* $z = 0$ *(c).* $\alpha = 45°$, $H_{coil1} = 3.0$ *mm,* $r_{coil1} = 0.8$ *mm and* $N_{turns \ coil1} = 15$. $H_{coil2} = 3.0$ *mm,* $r_{coil2} = 0.9$ *mm and* $N_{turns \ coil2} = 15$.
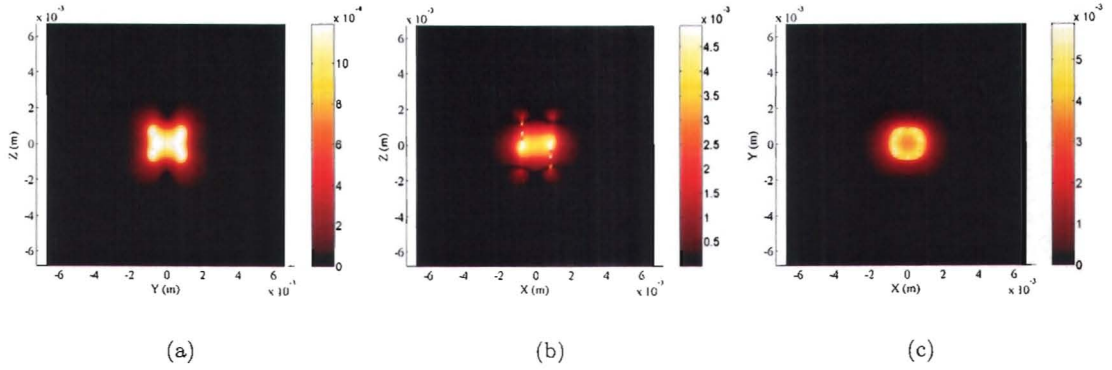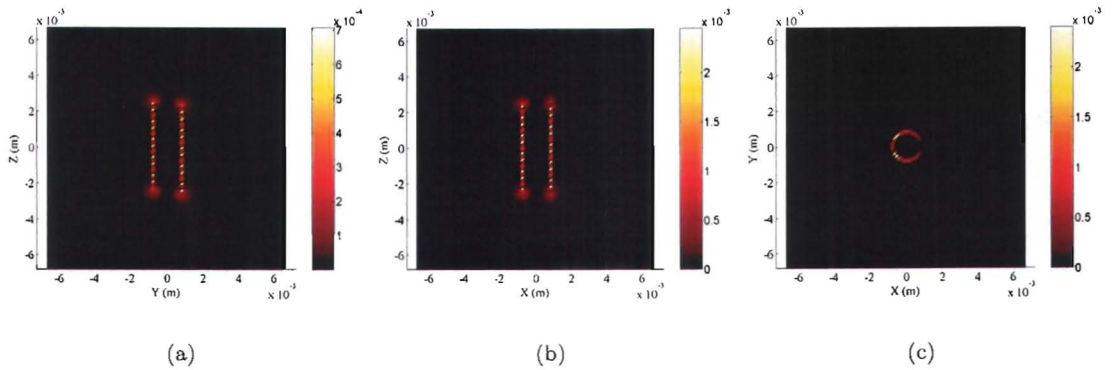

(a)   (b)   (c)

Figure 3.16: *Sensitivity pattern* $\left[\frac{T}{A} \cdot 10^{-1}\right]$ *of the solenoid coil in the xz plane at* $y = 0$ *(a), in the yz plane at* $x = 0$ *(b) and in the xy plane at* $z = 0$ *(c).* $H = 5.0$ *mm,* $r = 0.8$ *mm and* $N_{turns} = 15$.

23

3.3.3 Rotation

To test the orientation independence simulations were performed with different angles for rotation angle ϕ. The rotation ϕ is the angle of rotation around the x axis, with respect to the $\mathbf{B}_0$ field, which points in the defined z direction, figure 3.17. Here also a 0.01 mA DC current is supposed to flow through the antenna.

For these simulations the characteristics of the used coils were the same as in the previous simulations.

Results

Single coil with the 45° orientation with respect to the coil axis

The results of the sensitivity pattern in the xy plane at $z = 0$ with ϕ between 15° and 90° of one coils with the 45° orientation with respect to the coil axis are shown in figure 3.18(a) trough 3.18(f). The xy plane is shown because only changes in the xy plane can be measured by the MR scanner.

Figure 3.17: *Definition of ϕ.*

The amplitudes of the sensitivity patterns of one of the coils with the 45° orientation with respect to the coil axis, figure 3.18, first increases, from 15° trough 45°, and then decreases, from 60° trough 90°. From 15° trough 45°, the sensitivity pattern is highly localised in the center of the coil and does not spread much outside the coil, then from 60° trough 90° the sensitivity pattern becomes less localised and two peaks that are not in the center become visible.

Two perpendicular coils with the 45° orientation with respect to the coil axis

The results of the sensitivity pattern in the xy plane at $z = 0$ with ϕ between 15° and 90° for two perpendicular coils with the 45° orientation with respect to the coil axis, are shown in figure 3.19(a) trough 3.19(f).

In figure 3.19 the sensitivity patterns of the two perpendicular coils are combined. From 15° trough 45°, the amplitude of the sensitivity patterns also increases. The sensitivity patterns is very localised in the center of the coil and doe not spread much outside the coil. For ϕ varying from 60° trough 90°, the amplitude of the sensitivity patterns also decreases. The sensitivity pattern becomes less localised.

Solenoid

The results of the sensitivity pattern in the xy plane at $z = 0$ with ϕ between 15° and 90° are shown in figure 3.20(a) trough 3.20(f) for the solenoid coil made by Cordis.

The amplitude of the sensitivity patterns of the solenoid coil, figure 3.20 also increases for ϕ varying from 15° trough 45° and then decreases for ϕ varying 60° trough 90°. The localisation sensitivity pattern does the same. At 45° the sensitivity pattern is highly localised in the center of the coil and does not spread much outside the coil and at 0° and at 90° the sensitivity pattern is not localised in the center.
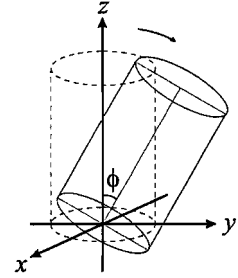
Discussion and conclusions

The coil with the 45° orientation with respect to the coil axis has an quite localised sensitivity pattern at all coil orientations. The coil can therefore probably be detected by the software of Philips quite well. The diameters of the sensitivity pattern are two to three mm, thus the depicted cross is expected to vary between two pixels. That variation is acceptable as explained in the previous subsection. Thus the coil is expected to be suited for active catheter tracking.

The two perpendicular coils with the 45° orientation with respect to the coil axis have a quite localised sensitivity pattern at all coil orientations. The amplitude of the sensitivity patterns is higher than the sensitivity pattern of one of the coils, because of the addition of the sensitivity patterns. The coils can therefore probably be detected by the software of Philips quite well, better than in the situation when one coil is used. The diameters of the sensitivity pattern are two to three mm, thus the depicted cross is expected to vary between two pixels. That variation is acceptable. Therefore the coil is suited for active catheter tracking, the results with these coils will probably be better than when one coil is used.

The sensitivity patterns of the coils with the 45° orientation with respect to the coil axis at the different rotation angles are more localised and have a higher amplitude than the sensitivity pattern of the solenoid coil. So the coils with the 45° orientation with respect to the coil axis can be detected more precise than the solenoid coil at the different orientation angles. The solenoid coil is therefore less suitable for active tracking.
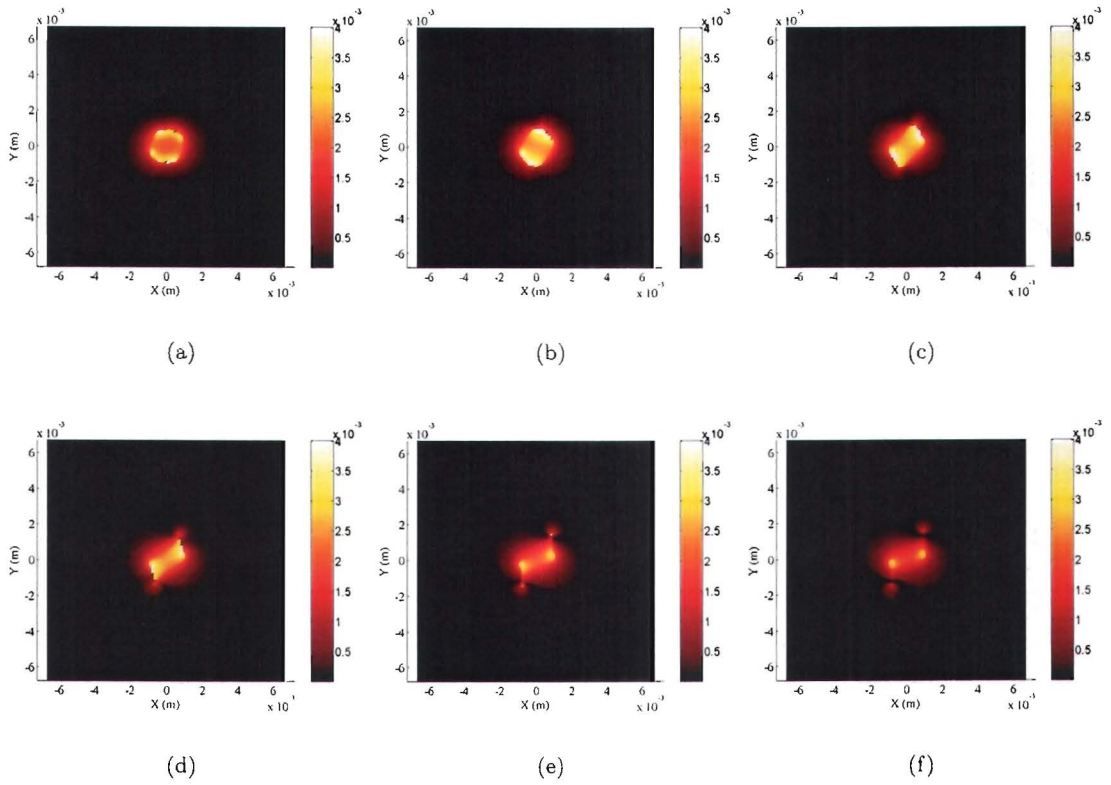
Figure 3.18: *The sensitivity pattern $\left[\frac{T}{A} \cdot 10^{-1}\right]$ in the xy plane at $z = 0$ of one coil with the 45° orientation with respect to the coil axis at 15° (a), 30° (b), 45° (c), 60° (d), 75° (e) and 90° (f) rotation around the x axis. $H_{coil1} = 3.0$ mm, $r_{coil1} = 0.8$ mm and $N_{turns\ coil1} = 15$.*

Figure 3.19: *The sensitivity pattern* $\left[\frac{T}{A} \cdot 10^{-1}\right]$ *in the xy plane at* $z = 0$ *of both perpendicular coils with the 45° orientation with respect to the coil axis at 15° (a), 30° (b), 45° (c), 60° (d), 75° (e) and 90° (f) rotation around the x axis.* $H_{coil1} = 3.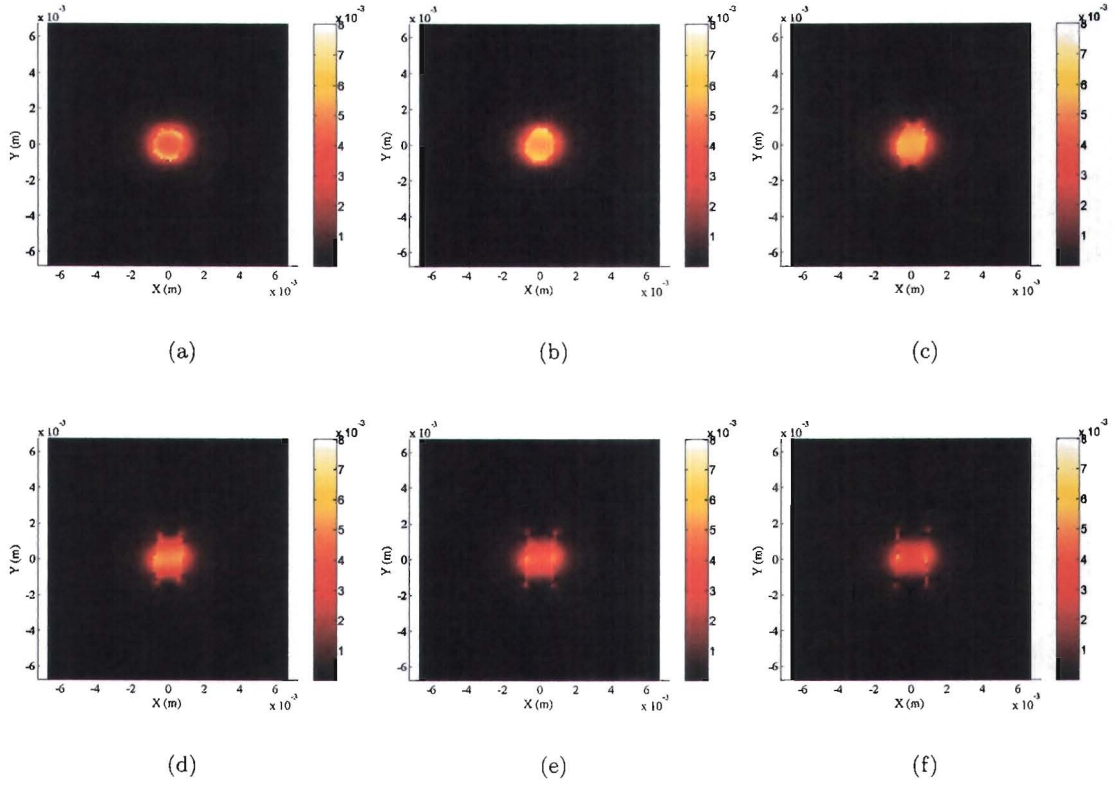0$ *mm,* $r_{coil1} = 0.8$ *mm and* $N_{turns\ coil1} = 15$. $H_{coil2} = 3.0$ *mm,* $r_{coil2} = 0.9$ *mm and* $N_{turns\ coil2} = 15$.

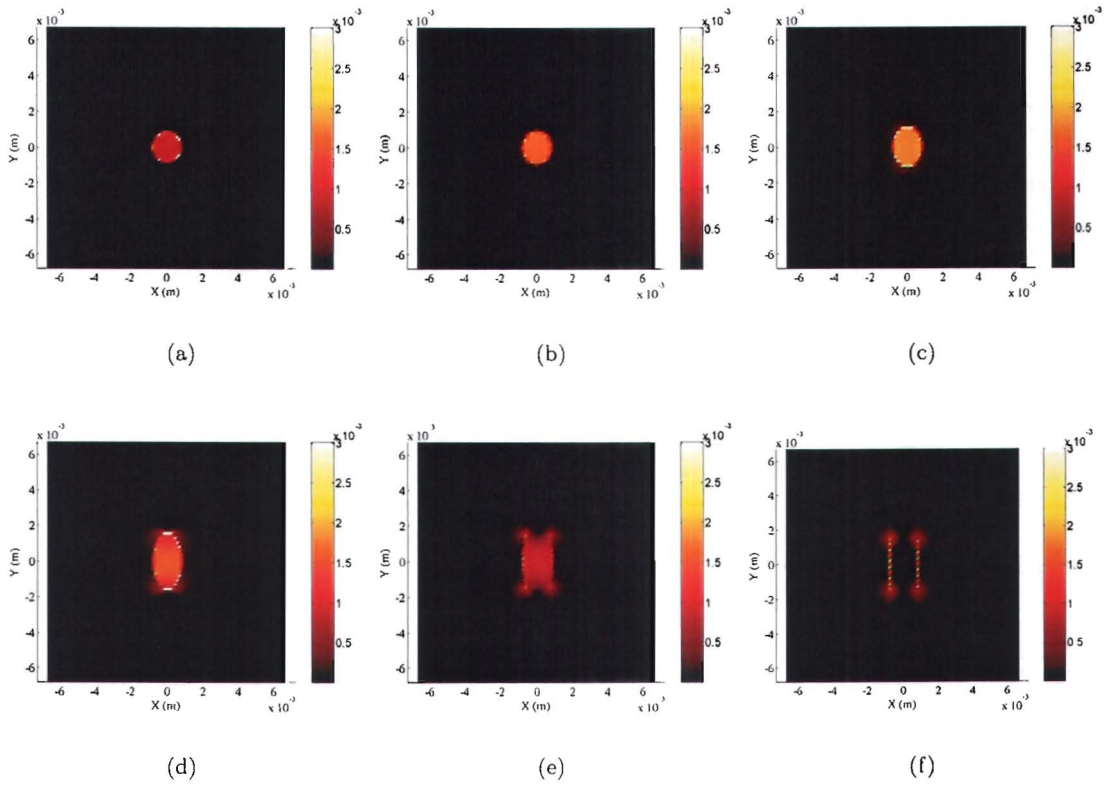Figure 3.20: *The sensitivity pattern* $\left[\frac{T}{A} \cdot 10^{-1}\right]$ *in the xy plane of at z = 0 the solenoid coil at 15° (a), 30° (b), 45° (c), 60° (d), 75° (e) and 90° (f) rotation around the x axis. H = 5.0 mm, r = 0.8 mm and $N_{turns} = 15$.*

3.4 In vitro experiments

3.4.1 Rotation

For the in vitro experiments only one of the two perpendicular coils with the 45° orientation with respect to the coil axis was used. Only one coil was used because it was too difficult to construct two perpendicular coils with the 45° orientation with respect to the coil axis by hand. The coil was wound according the configuration of figure 3.7 with 0.09 mm insulated copper wire. It had 15 windings and had a height of approximately 3.0 mm. The coil was glued to the tip a 5F (diameter is 1.67 mm) catheter. It was wound in the middle of the copper wire, so that when the coil was placed on the catheter both ends of the coil end in a copper wire with the length of the catheter. These ends were twisted, to minimise their influence on the B field, and attached along the catheter. At the end of the catheter, the 0.09 mm copper wire was soldered to a coaxial cable. The coaxial cable was connected to the "Catheter Preamp Box" of Philips.

The tip of the catheter was inserted in a rotatable phantom, figure 3.21. The used phantom was a box with two openings in two walls opposite to each other. The box was filled with an aqueous 19.2 mg/l $MnCl_2 \cdot 4H_2O$ solution, the lumen of the catheter was also filled with this solution during the experiments. The catheter was put in the box trough one of the openings and fixed in the center of the box with fishing wire. To test the orientation independence the box can be rotated, with angle ϕ with respect to $\mathbf{B_0}$. ϕ was defined in figure 3.17. The experiments were done at angles of 0°, 30°, 45°, 60° and 90°. The slice in which the the coil is situated was selected. An interactive scan with active tracking was performed.

Figure 3.21: *Rotatable phantom at* 0° *and* 45° *with respect to the direction of the main magnetic field* [5].

In the experiment the position of the coils was obtained by the hardware and software developed by Philips. The obtained positions were shown on the MR image. The experiment was done for approximately one minute per rotation angle. In this time domain all the measured positions of the coil were stored.

Results

The results are shown in figure 3.22 for the coil with the 45° orientation with respect to the coil axis and in figure 3.23 for the Cordis coil. Figures 3.22 and 3.23 show the measured positions of the depicted coil at pixel level, the squares in the figures represent the pixels of the MR image. The pixel size was 1.3722×1.3722 mm. The several measured positions are depicted by "+".

The measured positions of the coil with the 45° orientation with respect to the coil axis do not vary much. The measured positions of the solenoid coil vary much more. The average and maximum variation (in mm) in depicted positions of both coils is given in table. The
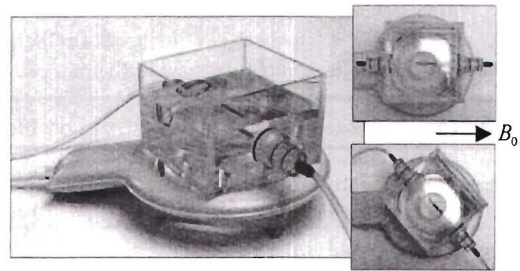
position where most crosses are is taken as "hotspot". The variation (v) is calculated as

$$v = \frac{\sum \sqrt{(x_i - x_0)^2 + (y_i - y_0)^2}}{\sum i} \tag{3.13}$$

where i is the number of the measurement, x_0 and y_0 are the x and y position of the hotspot, respectively, and x_i and y_i are the ith x and y position of the cross of which the variation is to be calculated.

Coil with the 45° orientation with respect to the coil axis			Solenoid		
Rotation	Average variation (mm)	Maximum variation (mm)	Rotation	Average variation (mm)	Maximum variation (mm)
0°	1.31	3.93	0°	0.72	3.49
30°	2.89	6.65	30°	0.08	0.23
45°	0.87	7.36	45°	0.13	0.42
60°	0.39	3.08	60°	0.22	0.48
90°	0.79	8.72	90°	0.28	0.78

Table 3.1: *The average and maximum variation in depicted positions.*

Discussion and conclusion

To obtain a good impression of the positions of the coil, the depicted position has to be stable. The positions of the coil with the 45° orientation with respect to the coil axis are more stable than the measured positions for the Cordis coil, see figures 3.22, 3.23 and table 3.1. The depicted positions of the coil with the 45° orientation with respect to the coil axis vary between three pixels, for $\phi = 0°$, two pixels, for $\phi = 45°$, $\phi = 60°$ and $\phi = 90°$ and for $\phi = 30°$ all measured positions are in one pixel. The few crosses at the left of the "hotspot" in figure 3.22(a), are assumed to be measurement errors. The variation in the depicted position of the catheter correpsonds with the expectations from the simulations.

For the Cordis coil many more pixels are used for the depiction of the position of the coil. These experiments lead to the conclusion that the the coil with the 45° orientation with respect to the coil axis was not orientation dependent. The depicted position of one coil was very stable. Therefore the coil with the 45° orientation with respect to the coil axis is quite suitable for active tracking.

When two perpendicular coils of this configuration are used inside each other the sensitivity pattern of the coils is more concentrated than when one coil is used, so the two coils are expected to give a similar or better result in the MR scanner. Assuming that the simulations and experiments correspond with each other like in the situation where one coil with the 45° orientation with respect to the coil axis is used, the depicted position of two coils will probably also be very stable and orientation independent. Therefore two coils with the 45° orientation with respect to the coil axis will probably be very suited for active tracking.

The depicted position of the Cordis coil is not as stable at all orientations as the the coil with the 45° orientation with respect to the coil axis. Therefore the Cordis coil is less suitable for active tracking.
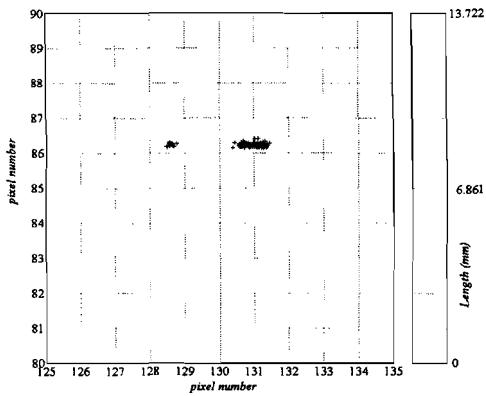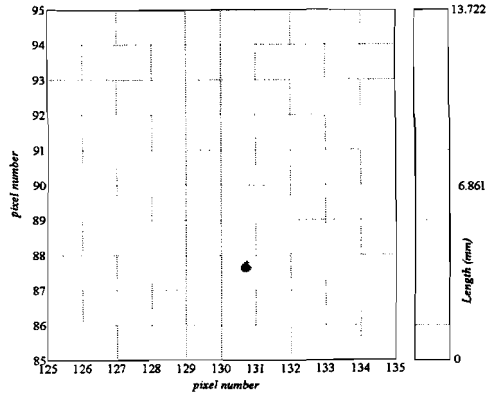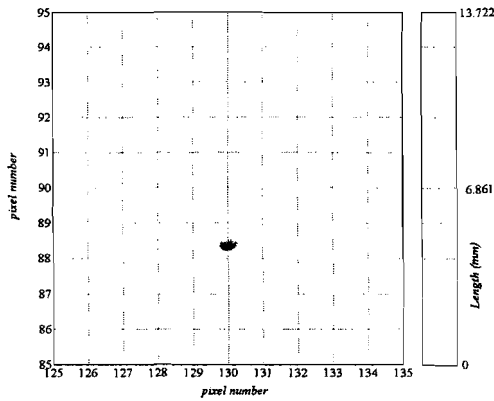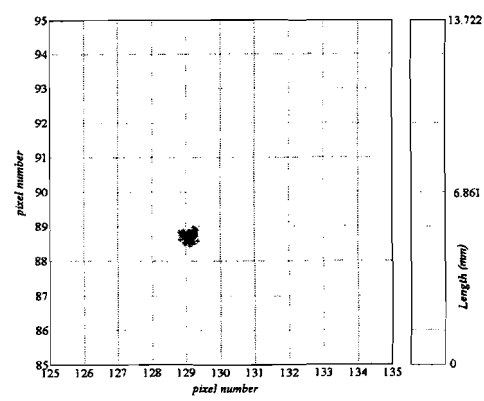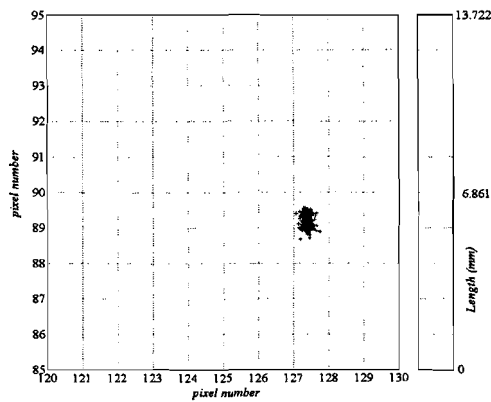
Figure 3.22: *Measured positions of the coil with the 45° orientation with respect to the coil axis at pixel level for $\phi = 0°$ (a), $\phi = 30°$ (b), $\phi = 45°$ (c), $\phi = 60°$ (d) and $\phi = 90°$ (e), obtained with the hard and software developed by Philips. Pixel size 1.3722 × 1.3722 mm.*
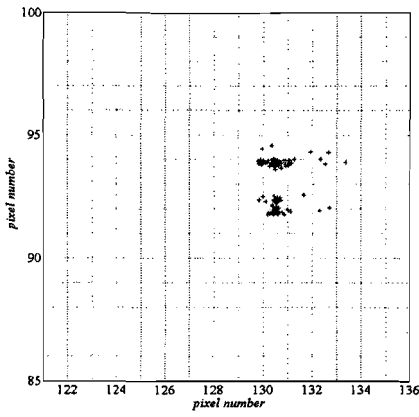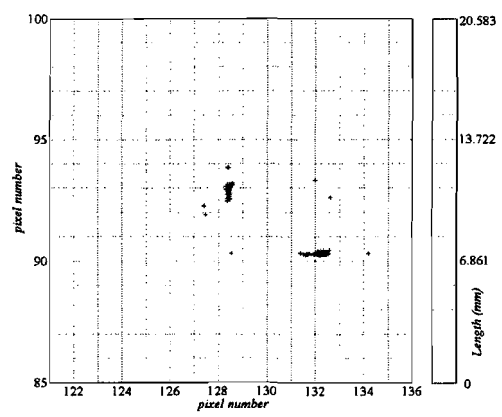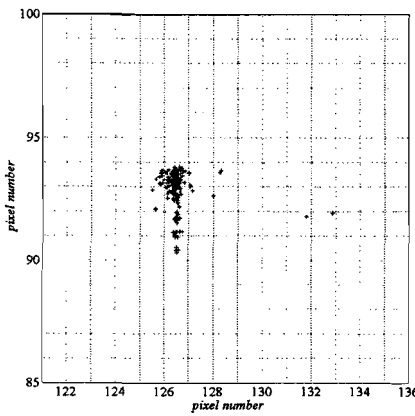
Figure 3.23: *Measured positions of the Cordis coil axis at pixel level for* $\phi = 0°$ *(a),* $\phi = 30°$ *(b),* $\phi = 45°$ *(c),* $\phi = 60°$ *(d) and* $\phi = 90°$ *(e), obtained with the hard and software developed by Philips. Pixel size* 1.3722×1.3722 *mm.*

3.4.2 Active tracking

To investigate whether the coil with the 45° orientation with respect to the coil axis is suitable for active tracking, the coil was inserted in a vascular phantom, fig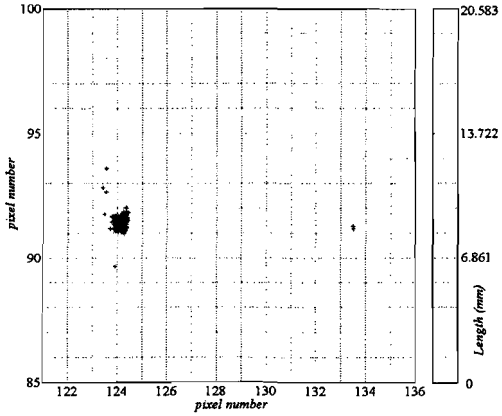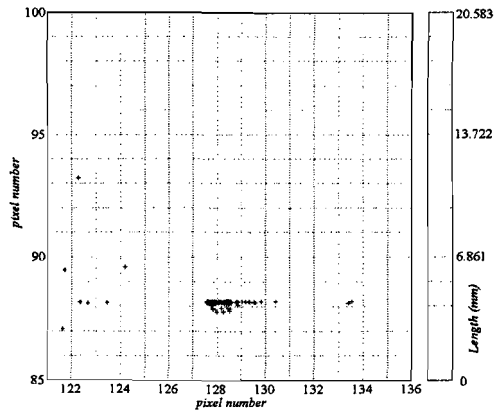ure 3.24. The used phantom was a massive silicone block with 19.2 mg/l $MnCl_2 \cdot 4H_2O$ solution filled vessels. The phantom has the vascular system of a human abdomen. The catheter was inserted via a guidewire in the phantom and guided through the vessels. The measured positions of the catheter are monitored.

Results

The position of the catheter is changed and the depicted position of the coil on the MRI scanner in monitored. This position moves along the vessel if the position of the catheter changes, see figures 3.24(a) trough 3.24(f), the white arrow does not belong to the MRI image but is just for clarity. At two heights in the vessel, the cross jumped out of the vessel in the horizontal plane, the vertical position did not alter, see figures 3.24(b) and 3.24(c). This jumping of the cross also occurred at these heights when the catheter is not moving.

Discussion and conclusions

The received signal in the vertical direction is constant and the received signal in the horizontal direction has different peaks. To give cause for this observed phenomenon, more experiments have to be carried out. The most likely cause is that the used antenna is not perfect. Now the supply wires are twisted by hand, it is likely that they cause distortions in the received signal. To solve this the wires can be replaced with a micro coaxial cable, as in the antenna Cordis designed. For an more ideal antenna, the coil has to be made more accurate. Now this is done by hand and the angle that the windings make with respect to the coil axis is probably not exactly 45° and the spacing between the windings is probably not constant. Then the above described experiment has to be repeated with the ideal antenna. When the phenomenon does not occur, the problem is caused by the fact that the antenna is not perfect.

Another possible cause is that the gradient fields are not ideal. To check this, the experiment should be repeated in a rotatable phantom. When the observed phenomenon appears, the phantom has to be rotated, so the orientation of the coil changes. When the jumping of the cross stops, the problem is caused by the gradient fields.

The software made by Philips looks for a peak in the received signal and at the highest peak it assumes as the position where the coil is located. We do not see the received signals and therefore can not verify that the detection is perfect.

Assuming that the instability of the cross is caused by the fact that the antenna is not perfect, the designed antenna configuration is very suitable for active tracking, provided that the tracking antenna is "ideal". The coil has to be attached to a cable that causes minimal disturbance, for example a micro coaxial cable. The coil has to be wound so that the angle that the windings make with the coil axis has to be exactly 45°. Due to safety aspects, the heating of the wires, the coil cannot be used for active tracking in patients and only be used for phantom and animal experiments.
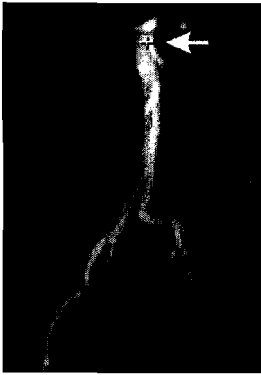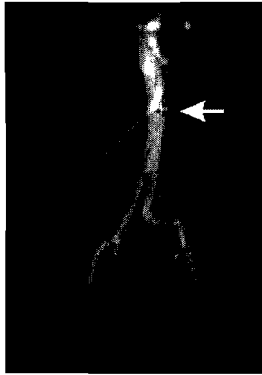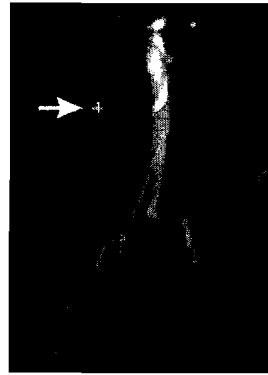
(a)   (b)   (c)
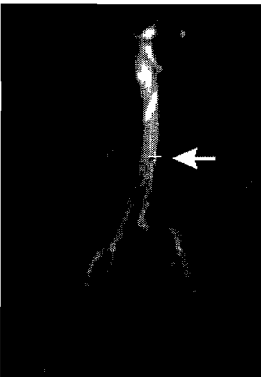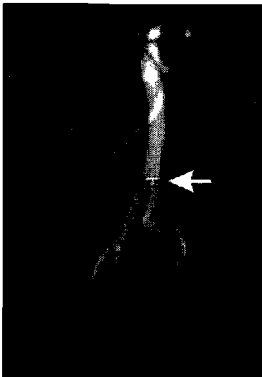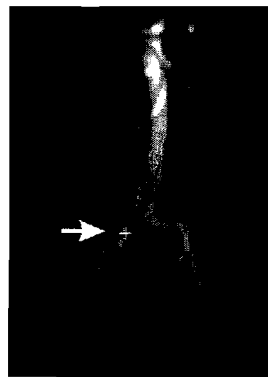
(d)   (e)   (f)

Figure 3.24: MR *images, made during active tracking, obtained with the hardware and software developed by Philips.*

Chapter 4

Safety aspects

The potential benefits of MRI are numerous; however, there are hazards intrinsic to the MR environment which must be acknowledged and respected. These hazards may be attributed to one or to a combination of the three main components that make up the MR environment: a strong static magnetic field (B_0) including its associated spatial gradient, pulsed gradient magnetic fields, and pulsed RF fields (B_1). For a properly operating system, the hazards associated with direct interactions of these fields and the body are negligible. It is the interactions of these fields with medical devices placed within the fields that create concerns for safety. The terms "MR safe" and "MR compatible" have to be defined when talking about hazards. When a device is "MR safe", the device, when used in the MR environment, has been demonstrated to present no additional risk to the patient, but may affect the quality of the diagnostic information [26]. When a device is "MR compatible", the device, when used in the MR environment, is MR Safe and has been demonstrated to neither significantly affect the quality of the diagnostic information nor have its operations affected by the MR device [26]. In table 4.1 a summary of the medical device concerns related to the MR environment is given [26].

In the following sections, each component of the MR environment is described. Subsequently, the heating problem is discussed in detail.

4.1 The static magnetic field and spatial gradient

B_0 is always present even when the MR scanner is not imaging. This field is typically between 0.2 and 2.0 T measured in the center of the magnet bore. Current technology is pushing this upper limit to 12 T in research MRI systems. This strong magnetic field strength drops off rapidly with distance away from the magnet, producing a large spatial gradient. As a result of this large gradient, magnetisable objects introduced into the field are accelerated and can quickly become dangerous projectiles. An example could be a pair of sharp scissors flying through the air pulled into the magnet bore.

Magnetic material aligns itself with the poles of a permanent magnet. Certain objects introduced into the MR environment will exhibit similar behavior. When brought near the magnet, these objects may be subjected to a torque which acts to align it with the magnetic field. This motion can be especially hazardous for certain implanted medical devices. In short, B_0 can induce a torque on an object whereas the associated spatial gradient can

Component of MR environment	Medical device concern	Potential adverse effect
Static magnetic field (B_0) (always on)	Rotation force (torque) on object	Tearing of tissues. Rotation of object in order to align with the field
Static magnetic field spatial gradient (always on)	Translation force on object	Tearing of tissues. Acceleration of object into bore of magnet "missile effect"
Gradient magnetic field (pulsed on)	Induced currents due to $\frac{dB}{dt}$	Device malfunction or failure
Radio frequency field (B_1) (pulsed during imaging)	RF induced current resulting in heating	Patient burns (thermal and electrical)
Radio frequency field (B_1) (pulsed during imaging)	Electromagnetic interference -active- device	Device malfunction induced noise (monitoring devices)

Table 4.1: MR *environment medical device concerns*

exert a translational force on the object. The magnitude of these effects depends on the geometry and mass of the object, as well as the characteristics of the MR system's magnetic field. Therefore, patients with certain implanted devices, such as many types of intracranial aneurysm clips, are contraindicated from MR imaging since the torque and displacement forces produced on the device can result in the tearing of soft tissues. Other implants, such as certain cardiac pacemakers are known to function erratically even in relatively weak magnetic fields. In device labelling for pacemakers, MRI is listed as a contraindication. Individuals with implanted pacemakers are contraindicated from entering the MR procedures room or coming within the 5 Gauss line around the scanner. In general, persons with any type of electrically, magnetically, or mechanically activated implants should remain outside the 5 Gauss line. The 5 Gauss line specifies the perimeter around the MR scanner within which the static magnetic fields are higher than five Gauss. The level of five Gauss and below are considered "safe" levels of static magnetic field exposure for the general public [26].

It is important to note that after processing a material, its magnetic properties may have been significantly altered. This change can be so significant that while the bulk material may be initially magnetically inert, once it is formed into a medical device, it may experience torque and translational forces significant enough to present a safety hazard when introduced in the MR environment. Therefore, all testing of devices for immunity to the strong static magnetic fields should be conducted on the device in its finished form. Quality assurance is especially important in order to insure that the behavior of a device in the MR environment does not vary significantly from item to item.

4.2 Pulsed gradient magnetic fields

When the gradient magnetic field is applied, the magnetic field intensity changes rapidly, giving rise to a time-varying magnetic field. During the rise time of the magnetic field, a voltage is induced in an electrical conductor, even when it is stationary in the field. However, in most MRI systems, the currents induced by the pulsed magnetic gradient field are about 1,000 times smaller than those induced by the pulsed RF component and are therefore not of great concern with regard to thermal injuries. Major concerns with the pulsed gradient fields are biological effects including electrical nerve stimulation and the generation of light flashes (magnetophosphenes) that may result from a slight torque exerted on the retinal cones in the eyes. Guidance limits the change in magnetic field intensity ($\frac{d\mathbf{B}}{dt}$) to levels which do not result in painful peripheral nerve stimulation.

4.3 Pulsed radio frequency fields

A third main component of the MR environment is the $\mathbf{B}_1$ field. With regard to biological effects, one main concern with this component of MR is the production of heat in tissue. The rate at which RF energy is deposited in tissue is defined as the specific absorption rate (SAR) which is measured in units of watts per kilogram $[W/kg]$ [26]. Guidance limits SAR whole body exposure. The duty cycle on the RF pulse during MR imaging is restricted based on this SAR limit.

With regard to medical devices, electrical currents may be induced in conductive metal implants, such as skull plates, and hip prostheses. When conductive patient leads are used during MR scanning, it is especially important that no loops are formed by the leads. Looped patient leads or devices pick up RF energy resulting in induced currents and heating of the material, which may results in potentially severe patient burns. To further reduce the possibility of burns, electrically conductive material in the bore of the magnet has to be insulated from the patient using blankets or sheets.

4.4 Heating problem

As described in the previous section, leads can heat up when placed in an MR scanner. This hazard has been described in literature frequently , for example [26, 20, 22]. When the line in the MR scanner is long ($\frac{\lambda}{2}$ or longer where λ is the wavelength in the surrounding medium) the line acts as a linear antenna and gets into resonance. Dissipation will take place at the tip of the wire that causes a temperature increase [20]. To possibly solve this problem, quarter wavelength chokes were used in the coaxial cable to avoid resonant lengths [2, 22]. Quarter wavelength chokes are used when a load is mismatched and a reflected wave exists on the line. It eliminates the standing wave at a certain frequency, there will be reflection at a slightly different wavelength [31].

When doing this the temperature increases are spatially distributed along the cable, so the peak temperature at the tip of the wire is reduced. This method requires application of extra coaxial layers, which can have consequences for the mechanical properties of the wire.

To gain a better understanding on this heating phenomenon, the resonant wire problem is modelled into two extremes. These models are first-order approaches, for which the resonance effects are easy to calculate. The reality is expected to be found somewhere between these

two extremes. In the first model the walls of the bore of the MR scanner are supposed to be non conducting. For the model, it is assumed that a conducting plate is placed at the bore of the MRI scanner. So the wire in the MR scanner can be modelled as a monopole antenna on a ground plane fed by a coaxial cable in a medium. This model is shown in figure 4.1.

In the second one the walls of the bore of the MR scanner is supposed to be a conductor. For the model, it is assumed that a conducting plate is placed at the bore of the MRI scanner. So the wire in the MR scanner can be modelled as two coaxial lines with a different inner and/or outer radius of the conductor. Because of this difference there is a coaxial discontinuity, which has to be regarded. This model is shown in figure 4.2.
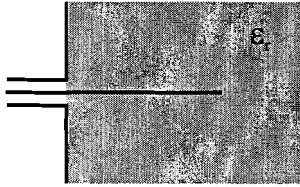

Figure 4.1: *The system modelled as a coax monopole junction.*
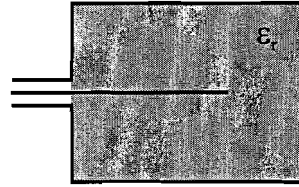

Figure 4.2: *The system modelled as a coax coax junction.*

For both models the input impedance of the junction is regarded as a function of the length of the line and the theory will be outlined in detail in the following two subsections. From the input impedance, one can conclude if and for what length the line is resonant. When the imaginary part of the input impedance is zero, the line is in resonance. The capacitance then is cancelled by the inductance and the input impedance is completely real. When the wire is in resonance no energy is stored, a oscillating current flows trough the wire, so the wire having a non zero distributed resistance gets warm. When the wire is resonant the dissipation at the tip of the wire will be maximal.

In the third subsection the models are compared. The frist-order models of the MRI scanner have been constructed to perform experiments to verify the calculations. The results of these experiments are shown in the last subsection of this chapter.

4.4.1 Coax monopole junction model

First, as shown in figure 4.1, it is assumed that a conducting plate is placed at the bore of the MRI scanner. Because of this conducting plate the wire inside the bore of the MRI scanner can be regarded as a monopole antenna on a ground plane. Than, for a better comparison with the real situation, it is assumed that the conducting plate is removed. For this situation the wire in the bore of the MRI scanner is a monopole on a ground plane of zero extent. For both situations the input impedance is regarded.

Situation with plate

First the coax monopole antenna junction was considered. A schematic representation of the junction of a coax to a monopole on a ground plane antenna is shown in figure 4.3. Z_{01} is the characteristic impedance of the coaxial cable. Z_L is the load impedance, in this case this is the input impedance of the monopole antenna, $Z_{in,\ m}$. The input impedance of a monopole
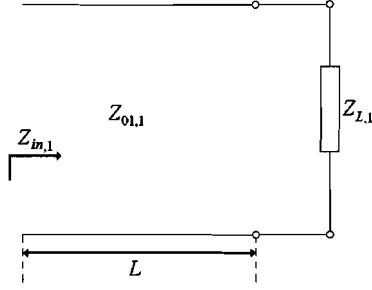
Figure 4.3: *The electrical circuit of the coax monopole junction.*

is given by the following equation [33, 37]:

$$Z_{in,\ m,1} = R_{in,\ m,1} + jX_{in,\ m,1} \tag{4.1}$$

where $R_{in,\ m,1}$ is the input resistance and $X_{in,\ m,1}$ is the input reactance of the monopole antenna. $R_{in,\ m,1}$ and $X_{in,\ m,1}$ for a monopole on a infinite ground plane are [33, 37],

$$R_{in,\ m,1} = \frac{\eta}{4\pi \sin^2(kl)} \left\{ Cin(2kl) + \frac{1}{2}\sin(2kl)\Big[Si(4kl) - 2Si(2kl)\Big] \right.$$
$$\left. + \frac{1}{2}\cos(2kl)\Big[2Cin(2kl) - Cin(4kl)\Big] \right\} \tag{4.2}$$

$$X_{in,\ m,1} = \frac{\eta}{4\pi \sin^2(kl)} \left\{ 2Si(2kl) + \cos(2kl)\Big[Si(2kl) - \frac{1}{2}Si(4kl)\Big] \right.$$
$$\left. - \sin(2kl)\Big[\ln(l/a) - Cin(2kl) + \frac{1}{2}Cin(4kl) + \frac{1}{2}Cin\Big(\frac{ka^2}{l}\Big)\Big] \right\} \tag{4.3}$$

where l is the length of the monopole and a is the radius of the monopole and,

$$\eta = \sqrt{\frac{\mu}{\varepsilon}} = \sqrt{\frac{\mu_r \mu_0}{\varepsilon_r \varepsilon_0}} \tag{4.4}$$

$$k = \frac{2\pi}{\lambda} \tag{4.5}$$

$$\lambda = \frac{c}{f\sqrt{\mu_r \varepsilon_r}} \tag{4.6}$$

where $c = 3.00 \cdot 10^8$ is the speed of light. f is the RF frequency. Here a 1.5 T MRI scanner is regarded, so $f = 64\ MHz$. ε_r is the relative permittivity of tissue. For blood $\varepsilon_r = 80$ [8]. $Si(x)$ is the sine integral,

$$Si(x) = \int_0^x \frac{\sin(t)}{t} dt \tag{4.7}$$

$Cin(x)$ is closely related to the cosine integral,

$$Cin(x) = \int_0^x \frac{1 - \cos(t)}{t} dt \tag{4.8}$$

40

Equations (4.2) and (4.3) are determined by using the method of images, where the monopole antenna may be modelled as a dipole with one half of the input impedance and twice the peak directivity of the dipole [4]. A sinusoidal current is assumed to flow trough the antenna. The ground plane is assumed to be of infinite extent. The equations are valid for thin elements ($ka < 1$) [33].
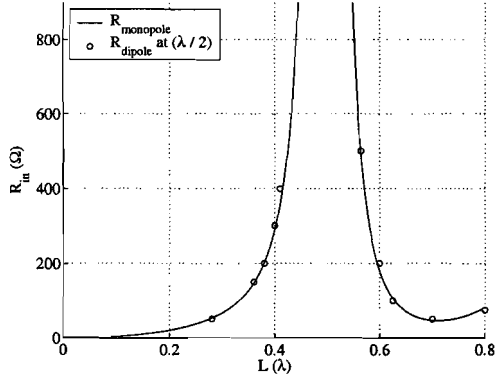

Figure 4.4: *Calculated $R_{in, m,1}$ as a function of λ of the monopole compared to R_{in} as a function of $\lambda/2$ of a dipole by Balanis [4].* $\mu = \mu_0$, $\varepsilon = \varepsilon_0$.
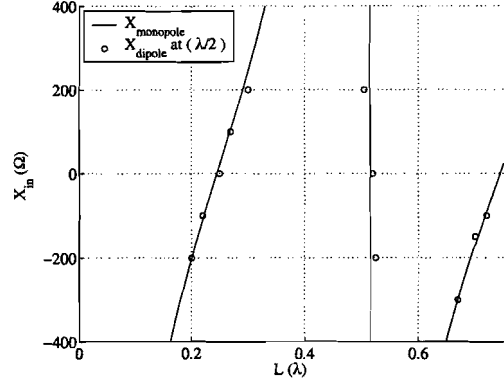

Figure 4.5: *Calculated $X_{in, m,1}$ as a function of λ of the monopole compared to X_{in} as a function of $\lambda/2$ of a dipole by Balanis [4].* $\mu = \mu_0$, $\varepsilon = \varepsilon_0$.

Graphs of the real ($R_{in, m,1}$) and imaginary ($X_{in, m,1}$) parts of the input impedance of the calculated monopole antenna on a infinite ground plane in free space are shown in figure 4.4 and 4.5. To verify for errors in the equations and errors in implementing these equations in FORTRAN code, the real ($R_{in, m,1}$) and imaginary ($X_{in, m,1}$) parts of the input impedance of the calculated monopole were compared with the real and imaginary part of the impedance of a dipole antenna in free space [4]. To make the comparison, the real and imaginary parts of the impedance values of the dipole antenna were divided by two and are taken at half the wavelength of the dipole [33]. This can be done because a monopole antenna on a ground plane can be regarded as a half dipole antenna. The real and imaginary part of the impedance of a dipole antenna in free space and the real ($R_{in, m,1}$) and imaginary ($X_{in, m,1}$) parts of the input impedance of the calculated monopole of the monopole antenna on a infinite ground plane in free space match, so it is valid to use the equations (4.2) and (4.3). The equations are implemented correctly in the FORTRAN routine.

The load impedance $Z_{L,1}$ shown in figure 4.3 is equal to $Z_{in, m,1}$ defined by equations (4.1) trough (4.8). The input impedance $Z_{in,1}$ of the the total coax monopole junction is given by the following equation,

$$Z_{in,1} = Z_{01,1} \left[\frac{Z_{L,1} + Z_{01,1} \tanh(\gamma_{1,1}L)}{Z_{01,1} + Z_{L,1} \tanh(\gamma_{1,1}L)} \right] = R_{in,1} + jX_{in,1} \qquad (4.9)$$

where L is the length of the coaxial cable, see figure 4.3, and γ_1 is the propagation constant of the coaxial cable,

$$\gamma = \omega \sqrt{\mu \varepsilon} \qquad (4.10)$$

41

Results

Graphs of the real part of the impedance $R_{in,1}$ and the imaginary part of the impedance $X_{in,1}$ as a function of the length L in wavelength λ, are shown in figure 4.6. The radius of the monopole is assumed to be 0.5 mm, this is assumed to be a realistic value. λ can be calculated with equation (4.6), here $\lambda = 0.524\ m$. The regarded coaxial cable has a $Z_{01,1}$ of 50 Ω.

Discussion and conclusion

In figure 4.6, when the imaginary part of input impedance is small, the real part of the impedance is maximal. When $X_{in} \neq 0$ there is no resonance, in this situation the lengths at which $|\Gamma|$ is minimal are regarded as "resonance" lengths [1]. The absolute reflection coefficient $|\Gamma_1|$ is shown in figure 4.7. $|\Gamma_1|$ can be calculated as follows:

$$|\Gamma_1| = \left| \frac{Z_{L,1} - Z_{01,1}}{Z_{L,1} + Z_{01,1}} \right| \tag{4.11}$$

$|\Gamma|$ is minimal when the monopole antenna is in "resonance". These "resonances" were found for lengths of approximately 0.4 λ, 0.6 λ, 0.9 λ, 1.1 λ, 1.4 λ, 1.6 λ and 1.9 λ. The monopole antenna is at the above mentioned lengths in "resonance", and the antenna will probably become heated for these lengths.
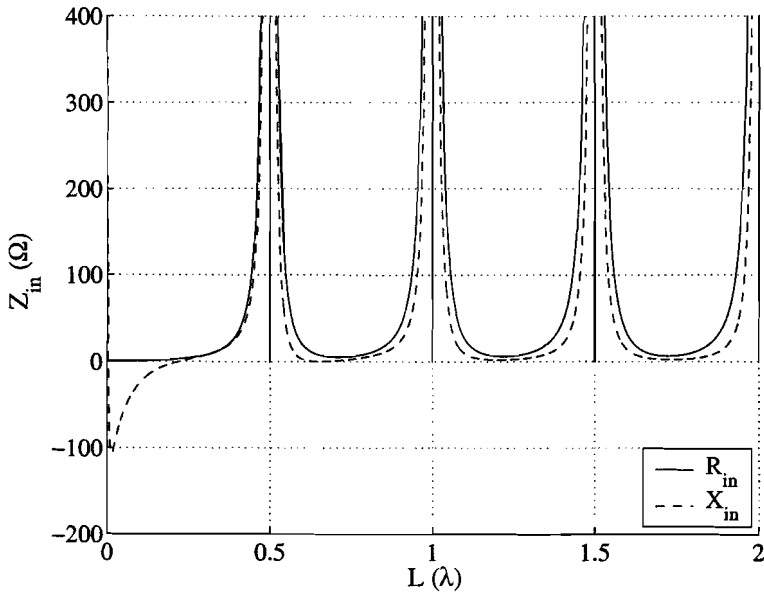
Figure 4.6: *Input impedance of the coax monopole junction.*
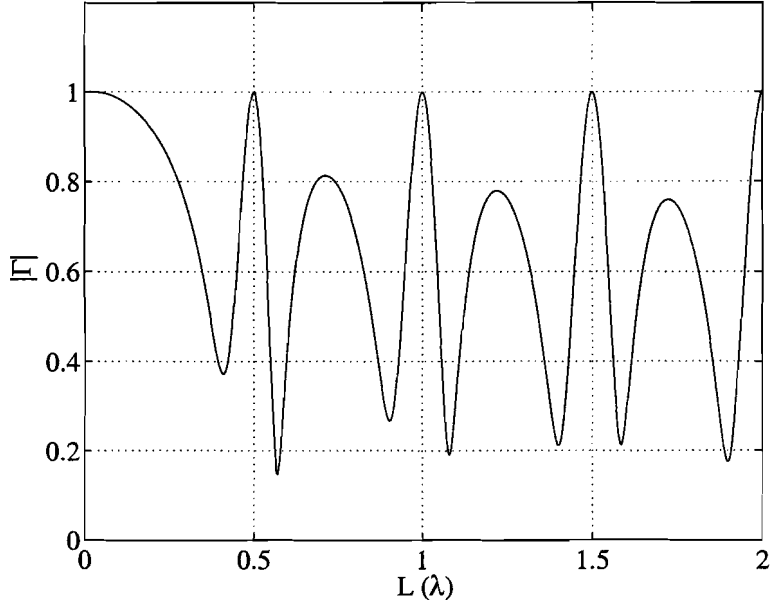
Figure 4.7: *Absolute reflection coefficient of the coax monopole junction.*

Situation without plate

Now, the situation is regarded where the conduction plate placed at the bore of the MRI scanner is removed. The junction can be modelled as a monopole antenna on a ground plane of zero extent, fed by a coaxial cable. The equations for the input impedance $Z_{in,\ m,2}$ for a monopole on a ground plane of zero extent is [33]:

$$Z_{in,\ m,2} = R_{in,\ m,2} + jX_{in,\ m,2} \tag{4.12}$$

with $R_{in\ m2}$ and $X_{in\ m2}$ given by,

$$
\begin{aligned}
R_{in,\ m,2} = \frac{\eta}{4\pi \sin^2(kl)} \Bigg\{ & Cin(x_1) + Cin(x_2) - 2Cin(x_3) \\
& + \frac{\sin(2kl)}{2} \left[\frac{(x_1 + x_2)(\cos(x_1) - \cos(x_2))}{x_1^2 + x_2^2 + 2x_3^2} \right] \\
& + \sin^2(kl) \left[\frac{(x_1 + x_2)(\sin(x_1) + \sin(x_2))}{x_1^2 + x_2^2 + 2x_3^2} - \frac{\sin(x_3)}{x_3} \right] \Bigg\} \quad (4.13)
\end{aligned}
$$

43

$$X_{in,\ m,2} = \frac{\eta}{4\pi \sin^2(kl)} \left\{ Si(x_1) + Si(x_2) - 2Si(x_3) \right.$$

$$- \frac{\sin(2kl)}{2} \left[\frac{(x_1 + x_2)(\sin(x_1) - \sin(x_2))}{x_1^2 + x_2^2 + 2x_3^2} \right]$$

$$\left. + \sin^2(kl) \left[\frac{(x_1 + x_2)(\cos(x_1) + \cos(x_2))}{x_1^2 + x_2^2 + 2x_3^2} - \frac{\cos(x_3)}{x_3} \right] \right\} \quad (4.14)$$

with

$$x_1 = k \left[(a^2 + l^2)^{\frac{1}{2}} + l \right]$$

$$x_2 = k \left[(a^2 + l^2)^{\frac{1}{2}} - l \right]$$

$$x_3 = ka$$

where l is the length of the monopole and a the radius of the monopole. η, k, $Si(x)$ and $Cin(x)$ are defined by equations (4.4), (4.5), (4.7) and (4.8) respectively.

Equations (4.13) and (4.14) are determined by the induced Electro Motive Force (EMF) method [28]. The EMF method is based on the fact that the power delivered by the source is used to maintain the current on the antenna. The power is calculated as the product of the current and the locally induced EMF, the electric field, this is explained in appendix B.

A sinusoidal current is assumed to flow trough the antenna. The ground plane is assumed to be of zero extent. The equations are valid for thin elements ($ka < 1$).
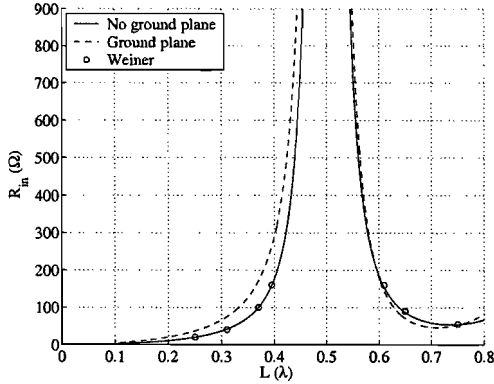
Figure 4.8: *Calculated $R_{in,\ m,2}$ as a function of λ of the monopole without the ground plane compared to $R_{in,\ m,1}$ as a function of λ of the monopole with the ground plane and the $R_{in,\ m}$ of an antenna with ground plane of zero extent calculated by Weiner et al. [33]. $\mu = \mu_0$, $\varepsilon = \varepsilon_0$.*
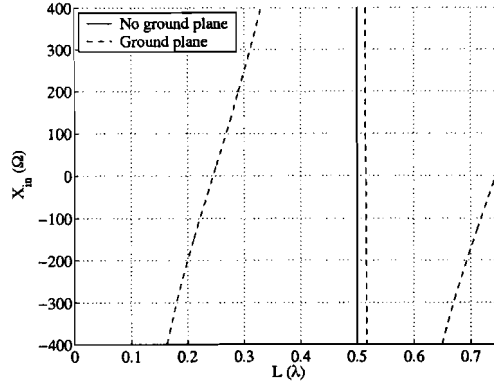
Figure 4.9: *Calculated $X_{in\ m,2}$ as a function of λ of the monopole without the ground plane compared to $X_{in\ m,1}$ as a function of λ of the monopole with the ground plane. $\mu = \mu_0$, $\varepsilon = \varepsilon_0$.*

In figure 4.8 the real part of the impedance of a monopole antenna on a infinite ground plane ($R_{in,\ m,1}$) and a ground plane of zero extent ($R_{in,\ m,2}$) is compared to values for a monopole antenna on a infinite ground plane calculated by Weiner [33]($R_{in,\ m}$), to validate the implementation of this equation in FORTRAN code. The real parts of the impedances of

44

the antenna with the infinite ground plane ($R_{in,\ m,1}$) and the antennas with the ground plane of zero extent ($R_{in,\ m,2}$ and $R_{in,\ m}$) have approximately the same form. The real parts of the impedances of the antennas with the ground plane of zero extent ($R_{in,\ m,2}$ and $R_{in,\ m}$) have the same values, so equation (4.13) is implemented correctly.

The imaginary part of the input impedance of the antenna with the ground plane of zero extent ($X_{in\ m,2}$) differs from the imaginary part of the input impedance of the antenna with the infinite ground plane ($X_{in\ m,1}$). The input impedance of the antenna of the antenna with the ground plane of zero extent ($X_{in\ m,2}$) has the same form as described by Weiner et al. [33]:

$$X_{in,\ m} = \begin{cases} -\infty & \text{for } kl \neq n\pi, \ n = 1, 2, 3, \ldots, \ a \to 0 \\ \\ \infty & \text{for } kl = n\pi, \ n = 1, 2, 3, \ldots, \ a \to 0 \end{cases} \qquad (4.15)$$

The calculated imaginary part of the impedance ($X_{in\ m,2}$) of the antenna with the ground plane of zero extent satisfies the definition given by Weiner ($X_{in\ m}$). So equation (4.14) is implemented correctly in the FORTRAN routine.

The input impedance, $Z_{in,2}$, of the total coax monopole junction is given by the following equation [31]

$$Z_{in,2} = Z_{01,2} \left[\frac{Z_{L,2} + Z_{01,2}\tanh(\gamma_{1,2}L)}{Z_{01,2} + Z_{L,2}\tanh(\gamma_{1,2}L)} \right] = R_{in,2} + jX_{in,2} \qquad (4.16)$$

Results

Graphs of the real part of the impedance $R_{in,2}$ and the imaginary part of the impedance $X_{in,2}$ as a function of the length in wavelength λ, are shown in figure 4.10. The radius of the monopole is assumed to be 0.5 mm. λ was calculated with equation (4.6), here $\lambda = 0.524\ m$. The regarded coaxial cable has a Z_{01} of 50 Ω.

Discussion and conclusions

In figure 4.10, when the imaginary part of the input impedance is zero, the real part of the input impedance is maximal. These resonances are found for lengths of is approximately 0.45 λ, 0.55 λ, 0.95 λ, 1.05 λ, 1.45 λ, 1.55 λ and 1.95 λ. The absolute reflection coefficient $|\Gamma|$ is shown in figure 4.11. $|\Gamma|$ is minimal when the monopole antenna is in resonance. The minimal values of $|\Gamma|$ are high, this means that the antenna is mismatched for 50 Ω.

This model is used because it resembles the real situation more than the model with the plate place in front of the bore of the MRI scanner. The monopole antenna is for the above mentioned lengths in resonance, and the antenna will probably become heated at these lengths. The lengths at which the monopole antenna with the ground plane of zero extent is in resonance do not differ much from the lengths at which the monopole antenna with the infinite ground plane is in resonance. So it is validated that the model of the monopole antenna on an infinite ground plane can be used instead of the model without the ground plane. The ground plane minimises the influence of currents on the outer conductor of the coaxial supply cable.
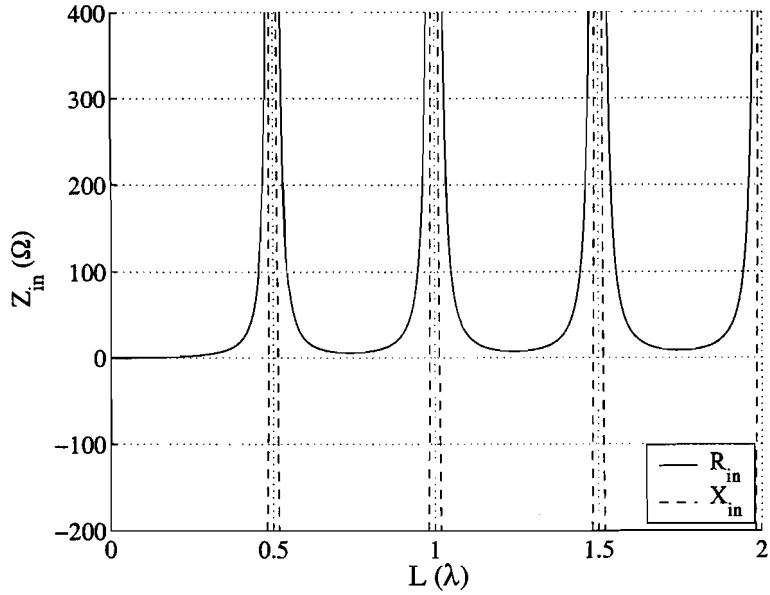
Figure 4.10: *Input impedance of the coax monopole junction.*
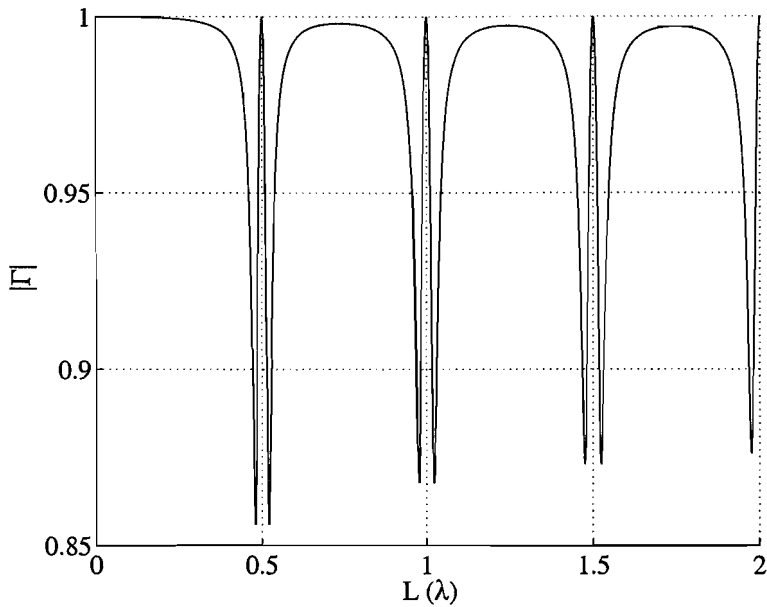
Figure 4.11: *Absolute reflection coefficient of the coax monopole junction.*

4.4.2 Coax coax junction model

A schematic representation of the junction of a coaxial cable to a differently dimensioned coaxial cable is shown in figure 4.12. $Z_{01,3}$ is the characteristic impedance of the coaxial cable on the left. C_{step} is the shunt capacitance due to the junction of two coaxial cables with
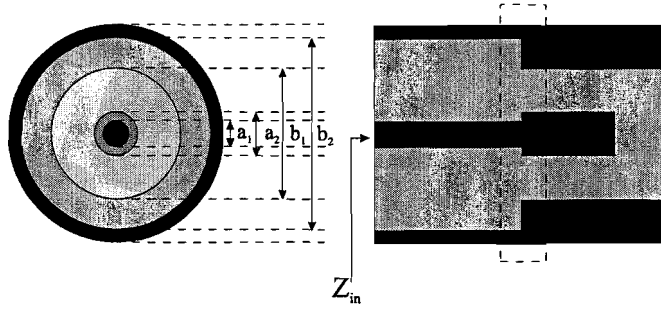
Figure 4.12: *The coax coax junction.*

different inner and outer conductor radii, see figure 4.13. $Z_{02,3}$ is the characteristic impedance of the second coaxial cable. To keep the theory as general as possible, we assumed that the length of inner conductor of the right coaxial cable is shorter than the length of the outer conductor of of the right coaxial cable, see figure 4.2. The coaxial cable on the right can be regarded as a coaxial line terminated in a circular waveguide. The equivalent circuit of this termination is a capacitor at the end of the line C_{term} [9]. Figure 4.13 is the equivalent electric circuit of the coax-coax- waveguide transition.
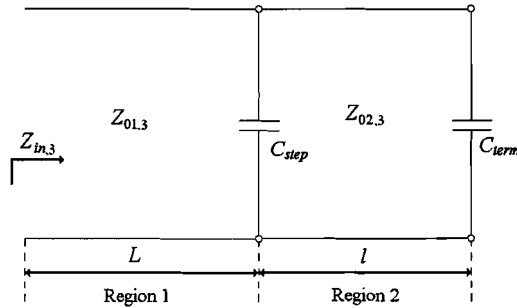
Figure 4.13: *The electrical circuit of the coax coax junction.*

The $Z_{0i,3}$ $(i = 1, 2)$ of a coax is [31]:

$$Z_{0i,3} = \sqrt{\frac{R_{i,3} + j\omega L_{i,3}}{G_{i,3} + j\omega C_{i,3}}} \qquad (4.17)$$

In equation (4.17) $R_{i,3}$ is the AC resistance per unit length of the coaxial cable comprising the line of the specific region. $L_{i,3}$ is the external inductance per unit length of the specific region. The effects of the internal inductance are negligible. $G_{i,3}$ is the conductance per unit length of the specific region due to the dielectric medium separating the conductors. $C_{i,3}$ is the capacitance per unit length of the specific region. $R_{i,3}, L_{i,3}, G_{i,3}$ and $C_{i,3}$ are given by [31]:

$$R_{i,3} = \frac{1}{2\pi\delta\sigma_c} \left(\frac{1}{a_i} + \frac{1}{b_i} \right) \qquad (4.18)$$

47

with

$$\delta = \frac{1}{\sqrt{\pi f \mu_c \sigma_c}} \tag{4.19}$$

$$L_{i,3} = \frac{\mu}{2\pi} \ln\left(\frac{b_i}{a_i}\right) \tag{4.20}$$

$$G_{i,3} = \frac{2\pi\sigma}{\ln(\frac{b_i}{a_i})} \tag{4.21}$$

$$C_{i,3} = \frac{2\pi\varepsilon}{\ln(\frac{b_i}{a_i})} \tag{4.22}$$

where σ_c and μ_c are the conductivity and the permeability of the conductors and a_i and b_i are the inner and outer radii of the coaxial cable. The conductors are regarded as perfect conductors, so $\sigma_c \to \infty$ $\mho/m$ and $\mu_c = \mu_0$. Perfect conductors are regarded to make a comparison with the results obtained for the monopole, which also is considered to be perfectly conducting. σ, μ and ε are the conductivity, the permeability and the permittivity of the dielectric medium, respectively. The values are chosen $\sigma = 0$ $\mho/m$, $\mu = \mu_0$ and $\varepsilon = \varepsilon_0$ are chosen for the left region and $\sigma = 0$ $\mho/m$, $\mu = \mu_0$ and $\varepsilon = \varepsilon_0 \varepsilon_r = 80\varepsilon_0$ [8] are chosen for the right region, the conductivity of blood is 0.8 $\mho/m$ [8] but since for the coax monopole junction a lossless dielectric was used, here also a lossless dielectric ($\sigma = 0$) is assumed to make the comparison between both situations possible. a_i and b_i are the radii of the inner conductor and outer conductor of the coaxial cable of a specific region, see figure 4.12.
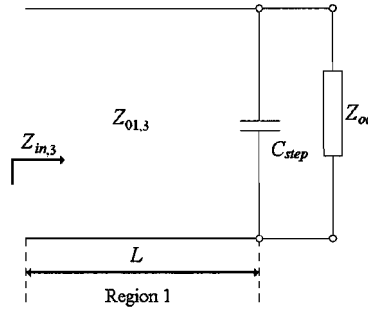
Figure 4.14: *The electrical circuit of the coax coax junction, when Z_{02} and the short circuit are combined.*

Values of C_{term} appear to be in the order 10^{-13} F [9, 30]. Because $Z_{02,3}$ has a low resistance and the frequency of a 1,5 T MRI scanner is 64 MHz, C_{term} can be neglected and the end of the line can be regarded as an open circuited line with impedance $Z_{L_{end}}$. The open end of the coaxial cable $Z_{L_{end}}$ and $Z_{02,3}$ can be combined into one impedance Z_{oc}, see figure 4.14 [31],

$$Z_{oc} = \lim_{Z_{L_{end}} \to \infty} Z_{02,3} \left[\frac{Z_{L_{end}} + Z_{02,3} \tanh(\gamma_2 l)}{Z_{02,3} + Z_{L_{end}} \tanh(\gamma_{2,3} l)} \right] = \frac{Z_{02,3}}{\tanh(\gamma_{2,3} l)} \tag{4.23}$$

with [31]

$$\gamma_{2,3} = \sqrt{(R_{2,3} + j\omega L_{2,3})(G_{2,3} + j\omega C_{2,3})} \tag{4.24}$$

48

where $R_{2,3}$, $L_{2,3}$, $G_{2,3}$ and $C_{2,3}$ follow from equations (4.18), (4.20), (4.21) and (4.22), respectively. The load impedance Z_L is the parallel connection of Z_{co} and C_{step},

$$Z_{L,3} = \frac{Z_{oc}}{j\omega\, C_{step}\, Z_{co} + 1} \tag{4.25}$$

The shunt capacitance C_{step} is caused by the step in two coaxial cables with a different inner and/or outer conductor diameter. The value of C_{step} appears to be in the order of 10^{-13} [15]. For the same reason that C_{term} may be neglected, C_{step} may be neglected, so $Z_L \approx Z_{oc}$. The input impedance $Z_{in,3}$ of the total system is given by the following equation,

$$Z_{in,3} = Z_{01,3} \left[\frac{Z_{L,3} + Z_{01,3}\tanh(\gamma_{1,3}L)}{Z_{01,3} + Z_{L,3}\tanh(\gamma_{1,3}L)} \right] \tag{4.26}$$

where L is the length of the left coaxial cable, see figure 4.14.

Results

A graph of The input impedance ($Z_{in,3}$) as a function of the length L is shown in figure 4.15. The real part of the impedance $R_{in,3}$ and the imaginary part of the impedance $X_{in,3}$ are shown as a function of the length L in wavelength λ. The outer radius of the left coaxial cable is calculated so that $Z_{01,3}$ equals 50 Ω. The radius of the inner conductor of the right coaxial cable is chosen to be the same as the radius of the inner conductor of the left coaxial cable, here the radius is 0.05 mm. The radius of the outer conductor of the right coaxial cable is taken to be 30 cm, being the radius of the MRI scanner. Here the plot of $|\Gamma|$ is not given, because it does not provide any additional information.
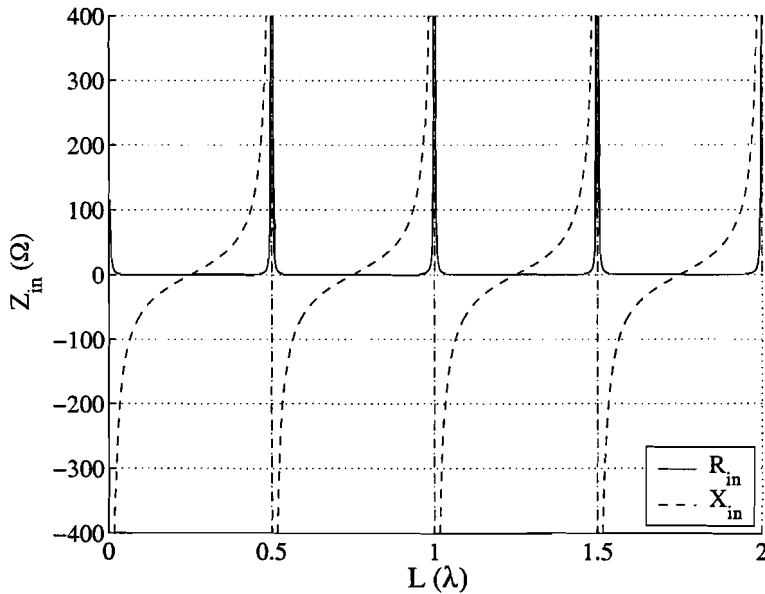

Figure 4.15: *Input impedance of the coax coax junction.* $\varepsilon_r = 80$.

Discussion and conclusions

In figure 4.15, when the imaginary part of the impedance is zero, the real part of the impedance is maximal, at lengths of 0.5 λ, 1.0 λ, 1.5 λ and 2.0 λ. Here the system is in resonance and therefore the cable and the surrounding tissue will probably be heated.

4.4.3 Comparison of the models

The real part of the impedances, figure 4.16, and imaginary part of the impedances, figure 4.17 as function of the monopole length for the monopole antennas and as function of the inner conductor length for the coaxial discontinuity, of the different models were compared. The models were assumed to be the two extremities. Since the walls of the bore of an MRI scanner are neither non perfectly conducting nor totally absent, the real situation of a wire in an MRI scanner is supposed to be in between these two extremes. The expected solution space for the real and imaginary part of the input impedance are the grey areas in figure 4.16 and 4.17 and show a relatively narrow area. Therefore the two extreme models may be useful in predicting the reality.
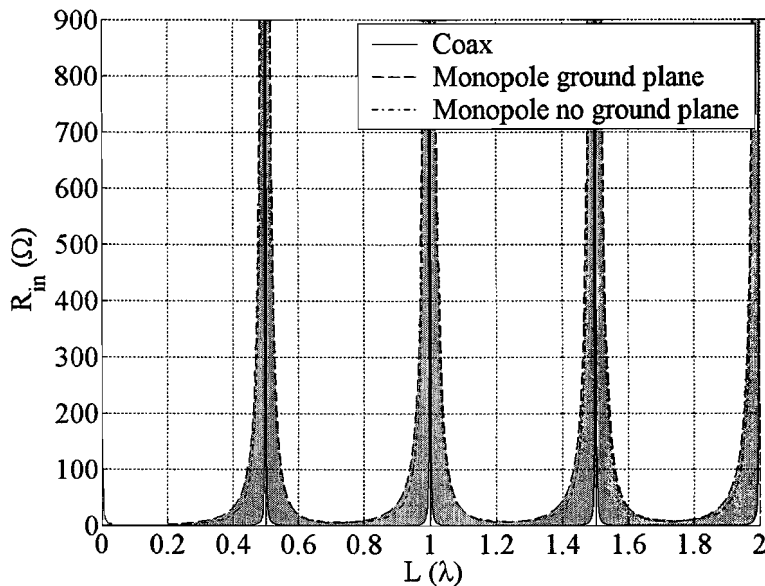
Figure 4.16: *Comparison of the real part of the impedances.* $\varepsilon_r = 80$.

The plots of the different situations do not differ much, the monopole antennas and the coaxial cable get in resonance at approximately the same values, around L is 0.5 λ, 1.0 λ, 1.5 λ and 2.0 λ. The values of the real and imaginary parts of the input impedance, R_{in} and X_{in}, for the wire in the MRI scanner will probably be in the grey parts of the figures between the two extremes. Because the three graphs do not differ much, the resonance of the real situation can be determined quite exact. For the verification of this, the experiments in the next subsection are performed for a situation between a monopole and a coaxial cable. This is done by putting a plastic cylinder around the monopole antenna, thus modelling a bore wall that is neither a perfect conductor nor totally absent. When the length of the wires is shorter than 0.4 times the wavelength in the used medium, the wires probably do not get in

50
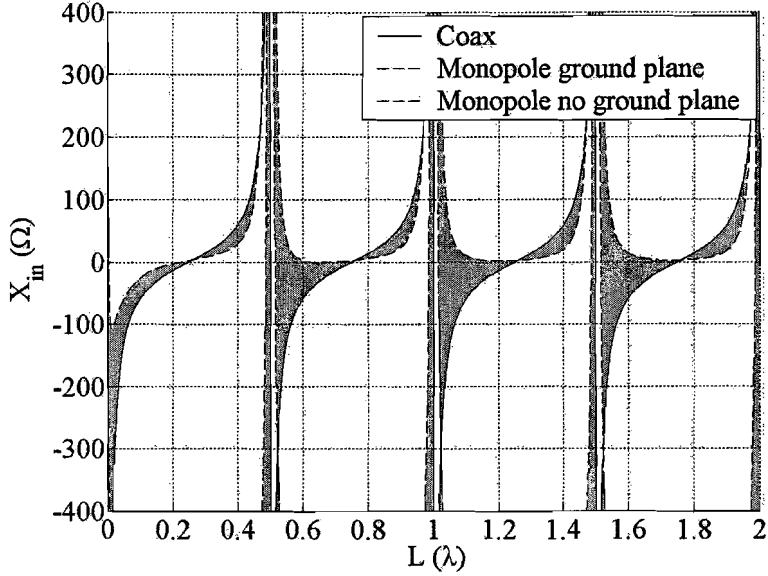
Figure 4.17: *Comparison of the imaginary part of the impedances.* $\varepsilon_r = 80$.

resonance, because the first resonance length is approximately 0.45 times the wavelength.

4.4.4 Experiments

Set- up with ground plate

A scale model of the MRI scanner and an insulated wire had been constructed, see figure 4.18. The wire was a coaxial cable that was fixed in the center of a round copper plate, the inner conductor of the coaxial cable sticks through the copper plate. The ground copper plate fitted precisely into a hollow copper cylinder. The wire trough the ground plate represented the monopole antenna on a ground plane. When the plate was fitted into the cylinder the coax coax junction is modelled. To verify a situation in between the copper cylinder and no cylinder, a plastic cylinder with an unknown ε_r was put over the monopole antenna.
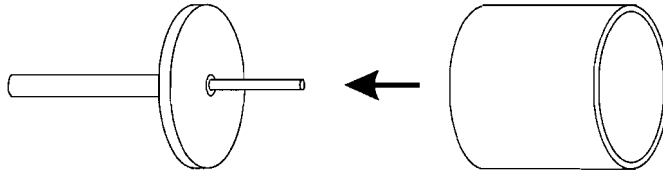
Figure 4.18: *Scale model of the MRI scanner and an insulated wire*

For the scale model the reflection coefficient was measured for different lengths of the inner conductor of the coaxial cable in the frequency range 8-12 GHz. This was done by cutting pieces of approximately 1 mm of the end of the inner conductor of the coaxial cable. The input impedance can be calculated from the reflection coefficient, Γ,

$$Z_{in} = Z_0 \left[\frac{1 + \Gamma}{1 - \Gamma} \right] \tag{4.27}$$

Z_0 is 50Ω.

The radius of the inner conductor is 0.45 mm, the radius of the outer conductor of the coaxialcable is 1.5 mm and the ε_r of the dielectric of the coaxialcable is 2.08, ε_r of air is 1. The radius of the copper cylinder is 3.3 cm and the radius of the plastic cylinder is 2.3 mm, the reason being that the plastic cylinder was not designed but laying around. The length of the coaxial cable, L in figure 4.3 and 4.13, is 8.20 cm.

Results

The plots of the reflection coefficients from the experiments are shown in figure 4.19 for the monopole antenna, in figure 4.20 for the monopole antenna with the copper cylinder (coaxial cable) and in figure 4.21 for the monopole antenna with the plastic cylinder. The experiments on the monopole model are compared with the calculated values of the monopole model. The experiments on the coaxial cable model are compared with the calculated values of the coaxial cable model. The experiments on the monopole model with the plastic cylinder are compared with the calculated values of the monopole model and the coaxial cable model.

Discussion and conclusions

In figure 4.19, the measured values do not coincide with the calculated ones, but the same length dependence is visible. The difference may be explained by the fact that in the equations a perfectly conducting infinite plate is assumed and in the experiment a copper plate with a 3.3 cm radius is used. Copper is a good but not perfect conductor. The wavelength of the waves at 10 GHz is 3 cm, so the used ground plane can hardly be assumed to be infinite. When the imaginary part of the impedance is minimal, the antenna is in resonance. So, in figure 4.19 can be seen that the resonance antenna is approximately 0.75 λ and 1.25 λ.

In figure 4.20, the measured values follow the calculated ones reasonably well. The differences may be attributed to the fact that because in the equations the conductors are assumed to be perfectly conducting and in the experiment a copper conductors are used. The configuration possesses very sharp resonance points, it is difficult to detect them exactly. Therefore, it is difficult to make a good graph of the measured points. For a better comparison more measurements have to be done with a smaller variation in length between two measurements. The imaginary part of the impedance is minimal when the length of the inner conductor of the right region is approximately 0.75 λ and 1.25 λ, here the configuration is in resonance.

In figure 4.21, the measured points follow the calculated line of the coax coax junction better than the calculated line of the coax monopole junction. For the real part of the impedance, the measured values are mostly in the grey area between the graph of the monopole and the coaxial line. Therefore, the monopole and coaxial line can be regarded as the two extreme situations for this problem. Not all measured values are in the grey area, this is because of the same reasons the measured values of the monopole antenna and the coaxial discontinuity do not match the calculated values perfectly. The imaginary part of the impedance is minimal when the length of the inner conductor of the right region is approximately 0.8 λ and 1.3 λ, here the set up is in resonance.
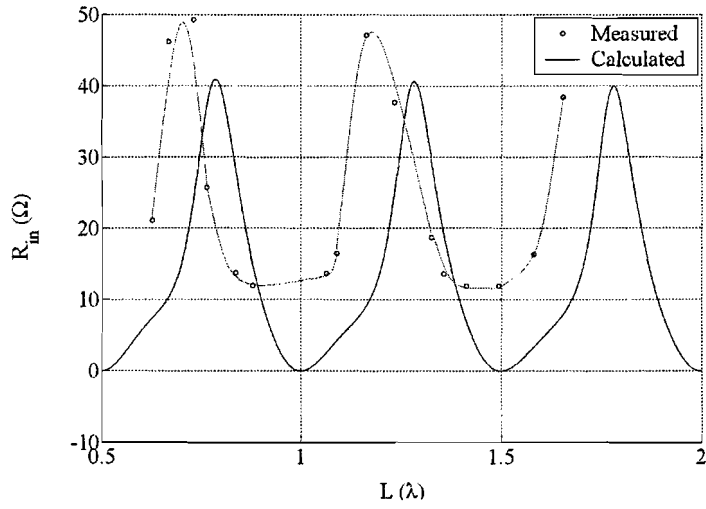
(a)
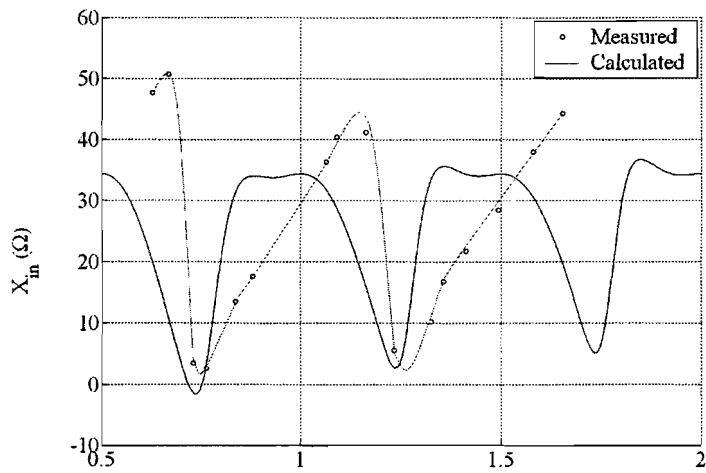
(b)

Figure 4.19: *Measured and calculated R_{in} (a) and X_{in} (b) of the experiment with the monopole with the plate at 10 GHz*

53

(a)

(b)

Figure 4.20: *Measured and calculated R_{in} (a) and X_{in} (b) of the experiment with the coaxial cable with the plate at 10 GHz*
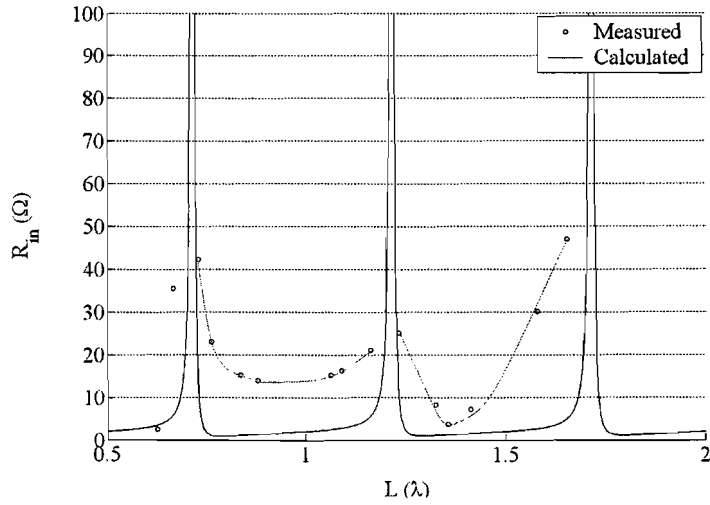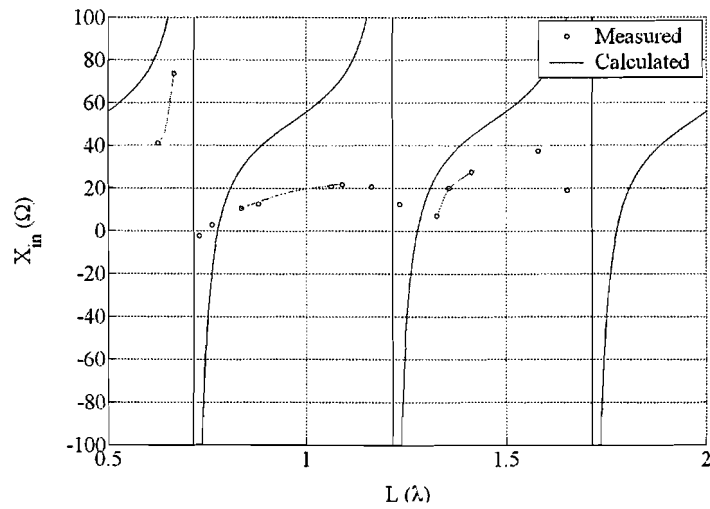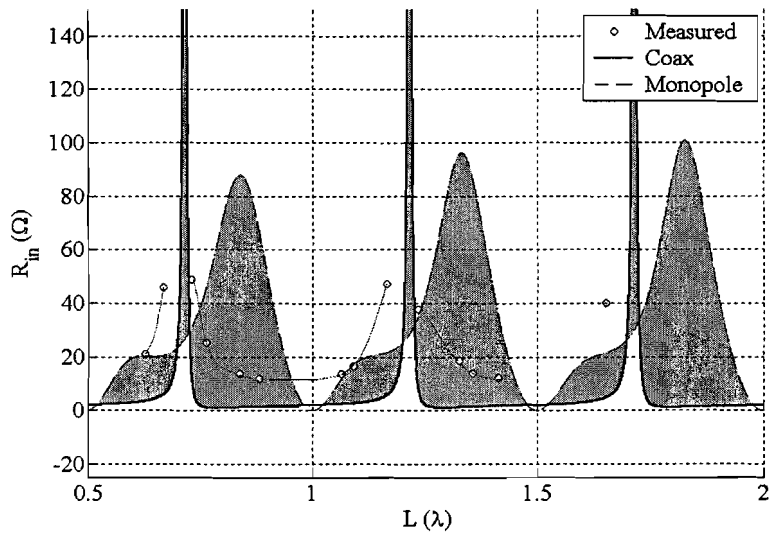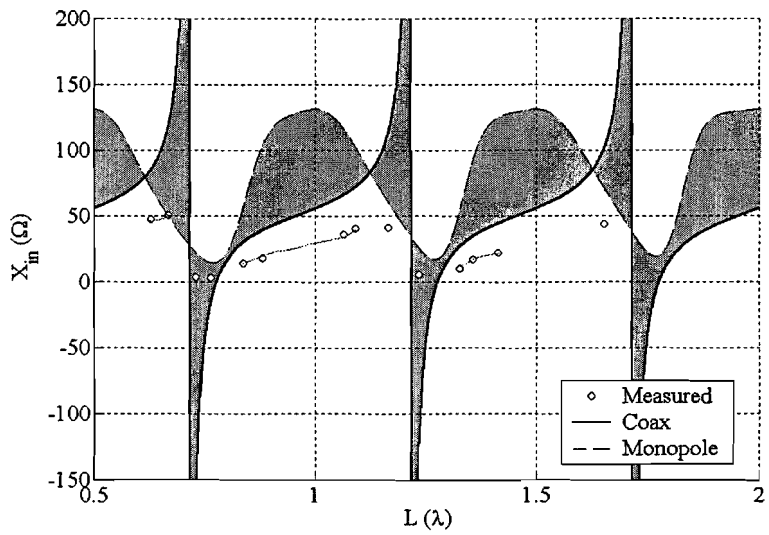
(a)

(b)

Figure 4.21: *Measured and calculated R_{in} (a) and X_{in} (b) of the experiment with the monopole on with the plate and the plastic cylinder at 10 GHz*

Set- up without ground plate

For a second experiment the round copper plate was removed, see figure 4.22. This represented the monopole antenna on a ground plane of zero extent. For the model of the coax coax junction without the plate, the inner conductor of the coaxial line was fixed in the center of the cylinder by putting polystyrene foam around it. Polystyrene foam has a permittivity of almost 1, so it did not affect the measurements. To evaluate a situation between the copper cylinder and no cylinder, a plastic cylinder with an unknown ε_r was used. Here the inner conductor was also fixed with polystyrene foam.
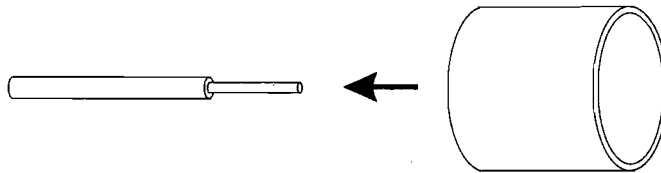

Figure 4.22: *Scale model of the* MRI *scanner and an insulated wire*

For these experiments, again the reflection coefficient was measured for the models for different lengths of the inner conductor of the coaxial cable in the frequency range 8-12 GHz. This was done by cutting pieces of approximately 1 mm of the end of the inner conductor of the coaxial cable. The radius of the inner conductor is 0.45 mm, the radius of the outer conductor of the coaxial cable is 1.5 mm and the ε_r of the dielectric of the coaxial cable is 2.08, ε_r of air is 1. The radius of the copper cylinder is 3.3 cm and the radius of the plastic cylinder is 2.3 mm. The length of the coaxial cable L in figure 4.3 and 4.13, is 4.95 cm.

Results

The plots of the reflection coefficients of the experiments are shown in figure 4.23 for the monopole antenna, in figure 4.24 for the monopole antenna with the copper cylinder (coaxial cable) and in figure 4.25 for the monopole antenna with the plastic cylinder. The experiments of the monopole model are compared to the calculated values of the monopole model. The experiments of the coaxial cable model are compared to the calculated values of the coaxial cable model. The experiments of the monopole model with the plastic cylinder are compared to the calculated values of the monopole model and the coaxial cable model.

Discussion and conclusions

In figure 4.23, the measured values do not coincide with the calculated ones or show the same length dependence. The difference may be explained by the fact that due to of the absence of a ground plane, the antenna becomes very sensitive for interference with the surrounding. Moreover, the currents in the outer conductor of the coaxial cable may radiate and contribute to the measured reflection. This last problem can be minimised by putting chokes at the end of the coaxial cable [4]. The imaginary part of the impedance is minimal when the length of the antenna is approximately 0.75 λ, here the antenna is in resonance.

In figure 4.24, the measured values follow the calculated ones quite good, for the imaginary part of the impedance even better than for the model with the ground plane. The small difference may be explained by the fact that in the equations the conductors are assumed to

be perfectly conducting and in the experiment a copper conductors are used. The imaginary part of the impedance is minimal when the length of the inner conductor of the right region is somewhere between 0.7λ and 0.8 λ, here the coaxial cable is in resonance. For a next experiment more measurements have to be taken, so the resonance points may be better determined.

In figure 4.25, the measured values follow the calculated ones of the coax coax junction better than the calculated ones of the coax monopole junction, for the imaginary part of the impedance better than the model with the ground plane. For the real part of the impedance, most measured values are outside the grey area between the two extremes. For the imaginary part of the impedance, almost all measured values are in the grey area between the two extremes. Not all measured values are in the grey area, this is because of the same reasons the measured values of the monopole antenna and the coaxial discontinuity do not match the calculated values perfectly. The imaginary part of the impedance is minimal when the length of the inner conductor of the right region is somewhere between 0.7λ and 0.8 λ, here the set up is in resonance. For a next experiment more measurements have to be taken, so the resonance point can than better be determined.
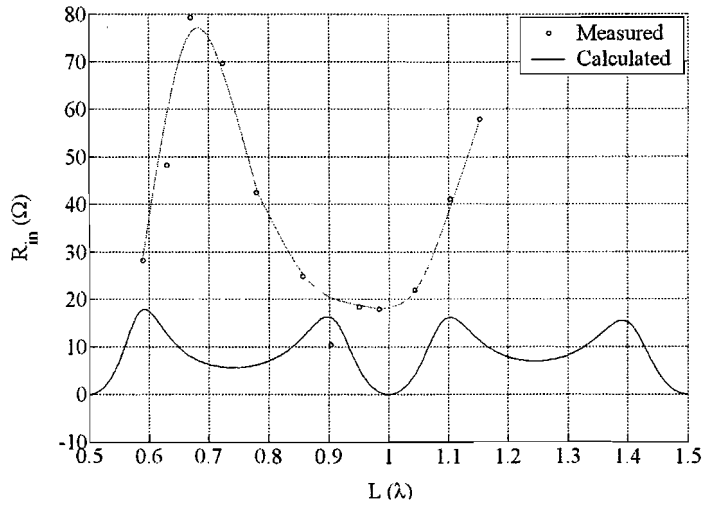
(a)
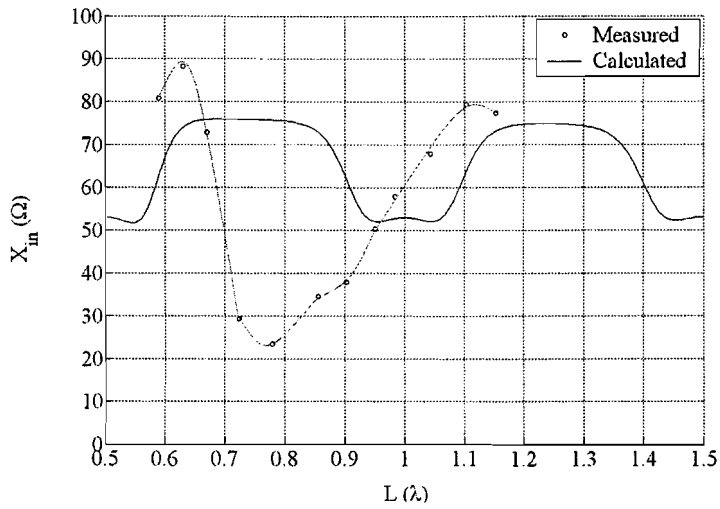
(b)

Figure 4.23: *Measured and calculated R_{in} (a) and X_{in} (b) of the experiment with the monopole without the plate at 10 GHz*

(a)

(b)

Figure 4.24: *Measured and calculated R_{in} (a) and X_{in} (b) of the experiment with the coaxial cable without the plate at 10 GHz*

(a)

(b)

Figure 4.25: *Measured and calculated R_{in} (a) and X_{in} (b) of the experiment with the monopole on without the plate and the plastic cylinder at 10 GHz*

Chapter 5

Further research

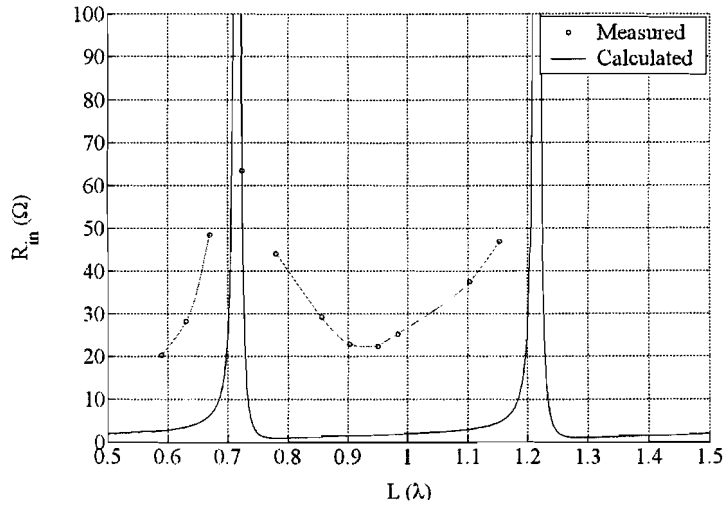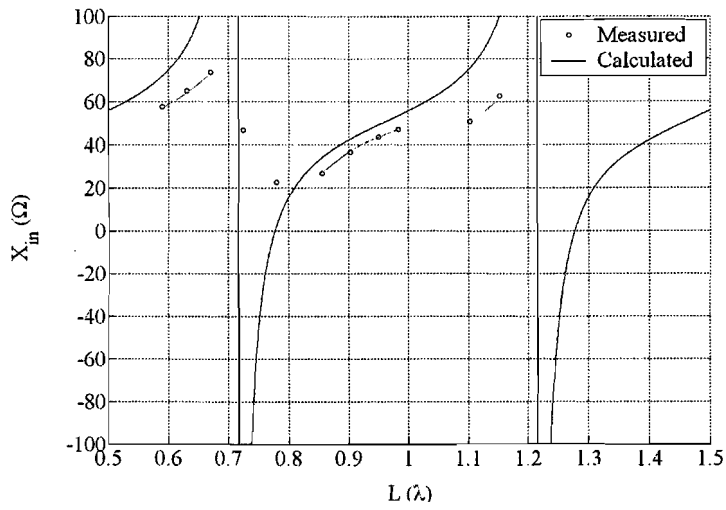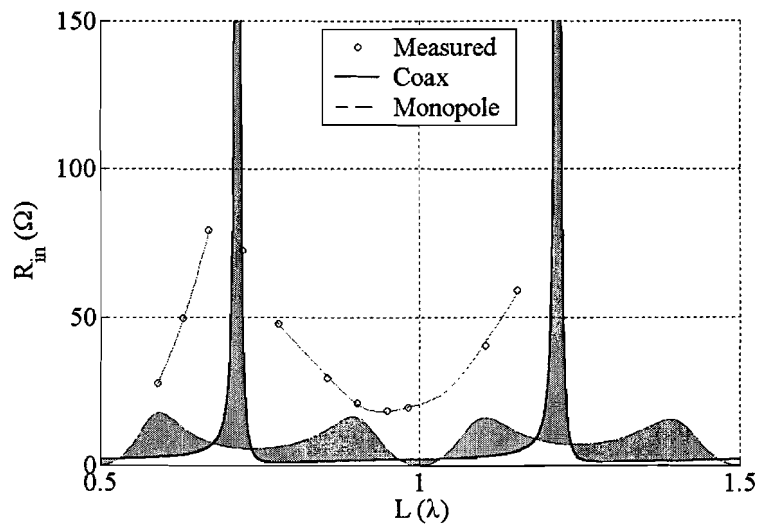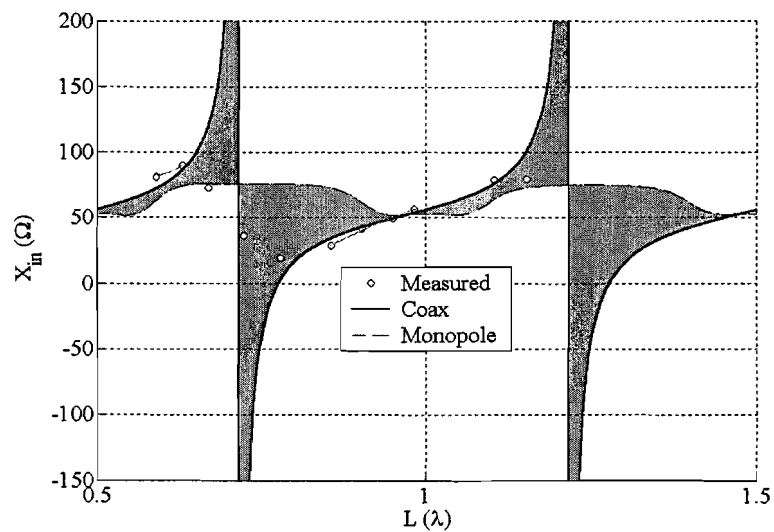Before active catheter tracking can be used in practice, a lot of research still has to be performed. In this chapter a few suggestions are given for further research in this field.

5.1 Optimisation

Optimisation may help in obtaining antenna configurations that meet the requirements best, if the optimum configuration is not obvious. For the used antenna configuration, the two perpendicular coils with the 45° orientation with respect to the coil axis, an a optimisation based on a Genetic Algorithm (GA) has been performed. The configuration that meets the requirement best is: small coils with as much windings as possible. The optimum of the used antenna configuration is quite obvious. For other antenna configurations, such as the micro coil with three separate winding elements as proposed by Zhang [40], figure 3.3, optimisation program will be handy. The optimum can be found with the help of a computer program, for example a program that works with a GA. An example of optimisation with GA is shown in this section.

GA optimises in analogy to natural selection and reproduction: A population of potential solutions (the parameters are codes as binary strings) to a problem is maintained and is repeatedly updated according to the principles of evolution: selection, mutation and/or crossover. Crossover selects pairs of solutions in the population (parents) and generates new solutions (children) by combining elements (parts of the binary strings) from their parents, which are then inserted in the population. The principle of selection demands that "good" solutions in the population are preferred in some way as compared to "bad" solutions. This can, for example be achieved by preferably selecting "good" solutions for reproduction, or by preferably letting "bad" solutions die. It is usually assumed that a fitness-function can be defined which assigns to each solution a number expressing "how good it is". Mutation modifies solutions in the population without interaction with the rest of the population. The algorithms used for crossover and mutation are usually formalised as binary operators which map one or two parents to a child [18].

5.1.1 Example

The coil designed by Zhang [40] is optimised using a software program that is based on a GA. The variables that are varied are the number of windings of each element (L_1, L_2 and L_3 in
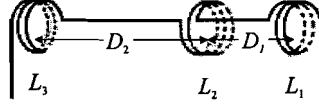
Figure 5.1: *The single coil design with unequally spaced elements ($D_2 > D_1$) designed by Zhang et al.*

figure 5.1) and the spacing between the elements (D_1 and D_2 in figure 5.1).

The number of windings and length of L_1, L_2 and L_3 are varied between 2 and 10. D_1 is varied between 3 mm and 8 mm, D_2 is varied between 1 mm and 3 mm. The radius of the windings is chosen as 0.8 mm, this is the radius of the catheter we used. The elements L_1 and L_3 are wound clockwise and L_2 is wound counter clockwise. The sensitivity patterns at the center of L_1, L_2 and L_3 are calculated (S_{L_1}, S_{L_2} and S_{L_3}) and the sensitivity patterns outside L_1, L_2 and L_3 are calculated (S_{O_1}, on the left of L_1, S_{O_2}, in between L_1 and L_2, S_{O_3}, in between L_2 and L_3, and S_{O_4}), on the right of L_3. The function (the fitness function F) that is maximised by the GA, is the following:

$$F = \frac{(S_{L_1} + S_{L_2} + S_{L_3})}{(S_{O_1} + S_{O_2} + S_{O_3} + S_{O_4})} \quad (5.1)$$

The program found the following values for the maximum of this function: 1 mm, 1 mm and 1 mm for the length of L_1, L_2 and L_3, respectively. 9, 6 and 10 for the number of windings for L_1, L_2 and L_3, respectively. 4 mm and 2 mm for D_1 and D_2

The sensitivity pattern of the optimised antenna is shown in figure 5.2. The sensitivity pattern shows three local peaks where the coils are situated, so the program optimised the sensitivity pattern of the antenna.
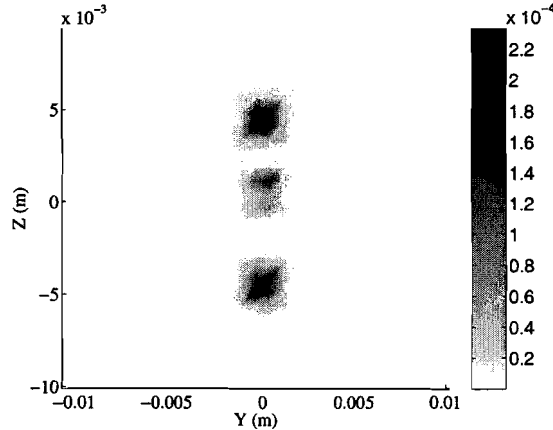
Figure 5.2: *Sensitivity pattern of $\left[\frac{T}{A} \cdot\right]$ in the yz plane at $x = 0$ of the optimised coil, designed by Zhang*

5.2 Sensitivity pattern
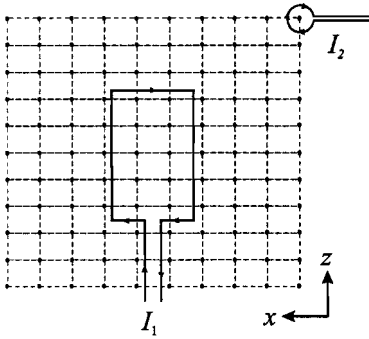
Figure 5.3: *An antenna in a two dimensional grid.*

Another suggestion for future research is to develop a measurement set up in which the sensitivity patterns of an antenna can be measured, without needing an MRI scanner. A current flows trough the antenna. This current induces a magnetic field around it. To measure this field, a three dimensional grid has to be applied. In figure 5.3, as an example, a two dimensional model of the system is shown. At every point of this grid the magnetic field has the be measured. This can be done by holding a coil (probe), here shown as one winding, at all the points. The magnetic field at the point induces a current trough the coil. When the current is measured at all points in the three dimension grid, the magnetic field at all points can be reconstructed with the Biot-Savart law.

The magnetic flux through the area enclosed by a circuit varies with time because of time-varying currents in nearby circuits. This process is known as mutual induction because it depends on the interaction of two circuits. The two coils, the antenna and the probe, are related to one another by a mutual inductance M [28]. With help of Faraday's law, M can be expressed as,

$$M_{12} = \frac{\int_{S_1} \mathbf{B}_2 \cdot \mathbf{dS}_1}{I_2} \tag{5.2}$$

where $\mathbf{B}_2$ is the magnetic flux arising from current I_2 and is integration over the surface of circuit 1. For isotropic materials, $M_{12} = M_{21}$. So the antenna is influenced by the field probe and vice versa.

The finite loop probe sustains not only the usual circulating current which is proportional to the normal magnetic field, but also certain other currents which do not depend on the normal component of the magnetic field, but rather on the average electric field in the plane of the loop. In practice, the probe can often be made small enough that these electric-field-dependent currents can be ignored [36].

5.3 Detecting resonance

Active catheter tracking is not safe with the present developments. The heating of wires in an MRI scanner is supposed to be due to resonance of the wires. A way to detect resonance in a wire may employ to a Rogowski coil.

Rogowski coils are used for measuring alternating currents. At resonance a AC current flows trough the wire in the MR scanner. Rogowski coils may be used to check if a wire in an MRI scanner is in resonance. A Rogowski coil measures the amplitude of a current. When the Rogowski coil is moved along the wire, the shape of the current is obtained. When a wire in in resonance the current is a standing wave [28]. This proposal needs further research.

Rogowski coils function by sensing the magnetic field caused by the current without making electrical contact with the conductor. An air cored coil is placed round the conductor in a toroidal fashion so that the alternating magnetic field produced by the current induces a voltage in the coil. The coil is effectively a mutual inductance coupled to the conductor being measured and the voltage output is proportional to the rate of change of current. This voltage is integrated electronically to provide an output that reproduces the current waveform [39],

$$v_{coil} = -\frac{d\Phi}{dt} = M\frac{di}{dt} \qquad (5.3)$$

with

$$M = \mu_0 N A \qquad (5.4)$$

Figure 5.4: *A Rogoswki coil*

where M is the mutual inductance, N is the number of evenly spaced turns per unit length, A is the cross-sectional area which encircles the conductor carrying current i and Φ the magnetic flux. A Rogowski coil is shown in figure 5.4 [39].

The addition of an integrator to the coil completes the transducer to provide a voltage which reproduces the current waveform. The characteristics of an integrator are described by an integration time constant $\tau = CR_s$. The output of the integrator, within the designed working bandwidth, is [39]

$$v_{out} = -\frac{1}{\tau} \int v_{coil} dt \qquad (5.5)$$

The output from the integrator can be used with any form of electronic indicating device such as a voltmeter, oscilloscope, protection system or metering equipment.

One of the most important properties of a Rogowski coil measuring system is that it is linear. The coil contains no saturable components and the output increases linearly in proportion to current right up to the operating limit determined by voltage breakdown. The integrator is also linear up to the point where the electronics saturates.

For accurate measurements using a Rogowski coil it is essential that the winding is extremely uniform when an air cored coil is used. The windings need to have a uniform spacing and the inner and outer radius of the coil should be equal. When the Rogowski coil is not extremely uniform, there is a DC offset. Figure 5.5 shows an uniformly wound Rogowski coil. When the **B** field is constant, the current trough the wire is as shown in figure 5.5. The induced current is dependent of the enclosed area of the segments. When the Rogowski coil is uniformly wound, the currents induced in the different line segments cancel each other. In figure 5.6 an extremely non uniform wound Rogowski coil is shown. Here the line segments do not have the same size, so the current induced in the different line segments are not equal and the current is not cancelled an a net DC current flows trough the Rogowski coil.

From Ampère's Law, with a perfectly uniform coil encircling a current, the output does not depend on the path the coil takes round the current or on the position of the conductor
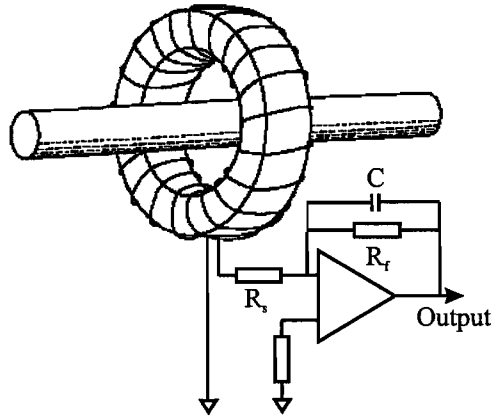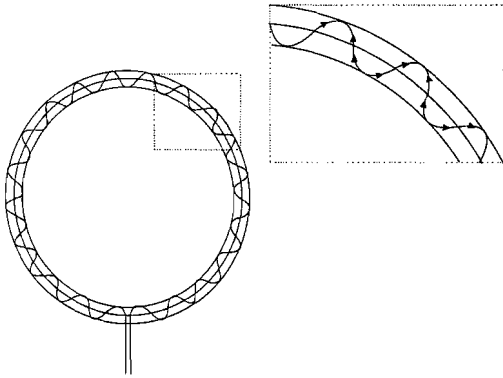
Figure 5.5: *Uniform wound Rogowski coil.*
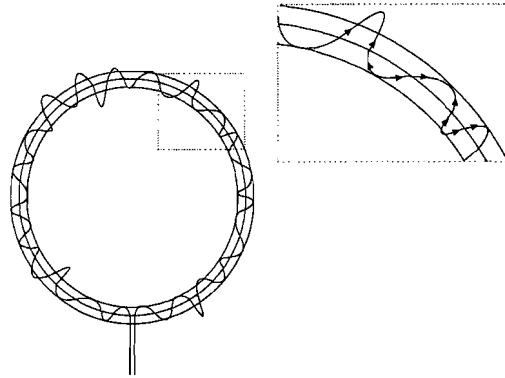
Figure 5.6: *Extremely non uniform wound Rogowski coil.*

within the loop. It is only necessary that the ends of the coil are brought together accurately. If the coil does not encircle a current the output is zero even if the coil is positioned near a current-carrying conductor.

5.4   Full wave Simulations

For the described simulations a static model is used. A static model neglects frequency dependence. The simulations of the monopole antenna on a infinite ground plane, the monopole antenna on a ground plane of zero extend and the coax discontinuity have to be performed with a full wave simulator, for example with Numerical Electromagnetic Code (NEC) [7]. NEC is considered here, because it is free to use. For the small intravascular antennas, Op den Kamp [19] verified that a static model may be used for the dynamic model.

NEC is more extensive that the static model. It takes influence of mutual interaction, caused by interaction of current carrying wires into account. The gauge of the wires is integrated in the model.

NEC can be used for the analysis of antennas. The program needs several input parameters, like a model of the antenna structure and the operation frequency. NEC obtains the current distribution. From these variables the input impedance and radiation pattern can be obtained. A model may include transmission lines, perfect or imperfect conductors, and lumped-element loading. NEC is built around the numerical solution of integral equations for the currents induced on the structure by sources or incident fields. The used numerical method is the Method of Moments. A structure may also be modelled over a ground plane that may be either a perfect or imperfect conductor.

NEC has some restrictions. The important ones are discussed here. NEC is only able to use free space. To overcome this restriction the frequency or the antenna size my be scaled to a blood environment. The wavelength corresponding to 64 MHz is [19]

$$\lambda = \frac{c}{f} = \frac{3 \cdot 10^8}{64 \cdot 10^6} = 4.69 \ m \tag{5.6}$$

The antenna should also be scaled so that the relation between the wavelength and the antenna is the same as in the blood environment. For comparison, in blood the wavelength

is 0.52 m. The frequency scaled to the blood environment [19],

$$f = \frac{c}{\lambda} = \frac{3 \cdot 10^8}{0.52} = 572 \ MHz \qquad (5.7)$$

A frequency of 572 MHz will give a situation in free space that is equivalent to the blood environment, assuming no losses.

NEC needs the antennas to be modelled by straight line segments. The coordinates of the start and end of the segments have to be given as input. There are restrictions to the lengths of the segments, $0.1 \ \lambda > l > 0.001\lambda$. The restrictions should be regarded to avoid numerical inaccuracy. The wire radius of the wire segments is also restricted. The wire radius is related to the wavelength, $\frac{2\pi a}{\lambda} \ll 1$, this has to be much smaller than 1, otherwise the validity of the approximations made in the model should be questioned. The accuracy for the current is also dependent on the ratio of the segment length to the wire radius, $\frac{l}{a}$. Reasonable current solutions are obtained for $\frac{l}{a} \geq 0.5$ [19].

Chapter 6

Conclusions

This project describes several aspects of active tracking in MRI. First some configurations for active tracking antennas are discussed, designed, simulated and tested. Then the safety aspects of active tracking are described. A wire in an MRI may cause heating of the surrounding tissue due to the dissipation of RF energy. This heating is caused by resonance. This problem is split into two extremes. The first order models of these extremes are discussed, simulated and tested.

For the active tracking several techniques are described in the literature [13, 25, 40, 11, 23]. Regarding the requirements for active tracking and due to some restrictions from the used software and hardware, designed by Philips, the technique that only detects the tip of the catheter is chosen to use in this project. For this technique, a coil is attached to the tip of the catheter. The signal of this coil is detected by the software of the Philips package and the measured position is projected on the MRI image.

A new antenna configuration is designed: two perpendicular coils with a 45° orientation with respect to the coil axis. This configuration is expected to be suited for active tracking, because the **B** field of the two coils is concentrated in the center of the configuration and for active tracking such a localised sensitivity pattern is desired. Weiss et al. [35] used this configuration for *fiducial markers*, they obtained good results. They showed that the configuration is orientation independent.

The sensitivity pattern of designed configuration is simulated and compared with the sensitivity pattern of a solenoid coil. Also the sensitivity pattern of one of the two perpendicular coils with the 45° orientation with respect to the coil axis is simulated and compared with the other two sensitivity patterns. The sensitivity pattern of a single coil with the 45° orientation with respect to the coil axis is localised and orientation independent. The sensitivity pattern of the two perpendicular coils with the 45° orientation with respect to the coil axis, which is in principle the addition of the two sensitivity pattern of the two coils, is also localised and orientation independent, the amplitude of the peak is higher than in the situation where one coil is used. The sensitivity pattern of the solenoid coil is not very localised for all catheter orientations.

The peak in the sensitivity patterns of the coils (one and two perpendicular) with the 45° orientation with respect to the coil axis is approximately 2 *mm* in diameter. This is due to the radius of the used catheter, which is related to the vessel diameter in which the catheter is inserted. Catheters with a radius of 0.8 are used in large (diameter 0.5-1.5 *cm*) veins and

arteries. The pixels of the MR imager are 1.3722 mm × 1.3722 mm. Thus the depicted cross is expected cover two pixels, for procedures in large vessels this is acceptable.

Therefore, one coil with the 45° orientation with respect to the coil axis is expected to be suitable for active tracking. The two coil configuration with the 45° orientation with respect to the coil axis is also expected to be suited for active tracking, even better than the situation where one coil is used. The solenoid coil is less suitable for active tracking, because the sensitivity pattern is not very localised and orientation dependent.

To verify these simulations, in vitro experiments have been performed. The catheter is inserted in a rotatable phantom and the position of the catheter is monitored on the MRI scanner at different angled with respect to the B_0 field. Because of the difficulty of making two perpendicular coils with the 45° orientation with respect to the coil axis only one of these coils is made and attached to a catheter. With the help of the hardware/software designed by Philips the orientation dependence of this coil is tested in vitro in the MRI scanner. These in vitro experiments are also performed on the solenoidal coil. The cross that visualises the position of the coil on the MRI images is reasonably stable when the coil with the 45° orientation with respect to the coil axis is used, the visualisation cross indeed jumps between two pixels. When the solenoid coil is used, a small variation in the position of the visualisation cross is visible. From these experiments it can be concluded that the coil with the 45° orientation with respect to the coil axis is orientation independent. The solenoid coil is less orientation independent.

According to this information, the coil with the 45° orientation with respect to the coil axis is quite suitable for active tracking. The solenoid coil is due to the orientation dependency and the less stable visualisation, less suitable for active tracking. Two perpendicular coils with the 45° orientation with respect to the coil axis will probably even be more suitable for active tracking than one coil with the 45° orientation with respect to the coil axis because the sensitivity pattern of the two coils is the superposition of the sensitivity patterns of the two separate coils. Considering the simulations and experimental results of one of the coils with the 45° orientation with respect to the coil axis, it is expected that the two coils will be detected correctly.

Another in vitro test is performed with the catheter with the coil with the 45° orientation with respect to the coil axis. The catheter is inserted in a vascular phantom and the catheter is guided trough the vessels and is monitored with the MRI scanner. This experiment showed good results, the catheter can be followed trough the vessels on the MRI scanner. Except at two heights, there the visualisation cross jumped out of the vessel, it remained at the right vertical position but not the right horizontal position. This problem is probably caused by the fact that the antenna and it supply cables are not ideal. But, despite this small problem, the used antenna is suited for active tracking.

The heating of a wire and the surrounding tissue in an MRI scanner is mainly caused by dissipation of energy, transmitted by the RF coils. The heating occurs when the wire is in resonance. To obtain a better understanding of this phenomenon, two first-order models of a wire in an MRI scanner that define the two extremes, are designed. The real situation is expected to be in between these two extremes.

By performing simulations with the obtained models, resonance of both models is regarded. The models appear to be resonant at approximately the same lengths. So the resonant lengths of a wire in an MRI scanner is expected to be approximated with help of the models, the length is expected to be in between the two extreme situations.

The simulations are compared with experiments. A scaled set up of both models is constructed. To verify if these two models are indeed the two extremes a set up of a situation in between those extremes is also constructed. In the experiments, the set ups appeared to be resonant at approximately the same lengths and results of the third situation appeared to be in between of the two extremes. So the modelled two extremes are indeed the boundaries of this problem. Because the two extremes become resonant at approximately the same lengths, the resonant length of a wire in an MRI scanner may probably be determined accurate. The get more accurate results the models should be expanded.

Bibliography

[1] D. Agahi and W. Domino. Efficieny measurements of portable handset antennas using the wheeler cap. *Applied Microwave and Wireless*, 2000.

[2] E. Atalar. Safe coaxial cables. In *Proceedings of the ISMRM 7th Scientific Meeting and Exhibition*, page 1006, 1999.

[3] C.J. Bakker, R.M. Hoogeveen, J. Weber, J.J. van Vaals, M.A. Viergever, and W.P. Mali. Visualisation of dedicated catheters using fast scanning techniques with potential for mr guided vascular interventions. *Magnetic Resonance in Medicine*, 36:816–820, 1996.

[4] C.A. Balanis. *Antenna Theory: Analysis and Design*. John Wiley & Sons, 1982.

[5] L.W. Bartels. *Magnetic Resonance Imaging for Guidance and Evaluation of Endovascular Therapy*. PhD thesis, Utrecht University, 2001.

[6] L.W. Bartels and C.J.G. Bakker. Endovascular interventional magnetic resonance imaging (topical review). *Physics in Medicine and Biology*, 48:R37–R64, 2003.

[7] G.J. Burke and A.J. Poggio. Numerical electromagnetic code documentation - part I: Program description theory. National Technical Information Service (U.S. Department of Commerce), Ordering codes: AD-A075 209, AD-A075 289 and AD-A075 460, 1997.

[8] M. Burl, G.A. Coutts, D.J. Herlihy, R. Hill-Cottingham, J.F. Eastham, J.V. Hajnal, and I.R. Young. Twisted pair RF coil suitable for locating the track of a catheter. *Magnetic Resonance in Medicine*, 41:636–638, 1999.

[9] J. Chramiec and J.K. Piotrowski. Universal formula for frequency-dependent coaxial open-end effect. *Electronic Letters*, 35(17):1474–1475, 1999.

[10] J.L. Duerk, E.Y. Wong, and J.S. Lewin. A brief review of hardware for catheter tracking in magnetic resonance imaging. *Magnetic Reconance Materials in Physics, Biology and Medicine*, 13:199–208, 2002.

[11] C.L. Dumoulin, S.P. Souza, and R.D. Darrow. Real-time position monitoring of invasive devices using magnetic resonance. *Magnetic Resonance in Medicine*, 29:411–415, 1993.

[12] F.E. Gardiol. *Introduction to Microwaves*. Artech House, 1984.

[13] A. Glowinsky, G. Adam, A. Bücker, J. Neuerburg, J.J. van Vaals, and R.W. Günther. Catheter visualisation using llocally induced, actively controlled field inhomogeneities. *Magnetic Resonance in Medicine*, 38:253–258, 1997.

[14] A. Glowinsky, J. Kürsch, G. Adam, A. Bücker, T.G. Noll, and R.W. Günther. Device visualisation for interventional MRI using local magnetic fields: Basic theory and its application to catheter visualization. *IEEE Transactions on Medical Imaging*, 7(5):786–793, 1998.

[15] L. Gogioso, M. Marchesi, and M. Parodi. A variational aproach to compute the equivalent capacitance of coaxial line discontinuities. In *Proceedings of the International Microwave Symposium*, pages 580–583, 1979.

[16] K.C. Gupta, R. Garg, and R. Chadha. *Computeraided Design of Microwave Circuits*. Artech House, 1981.

[17] B.P de Hon. Lecture notes elektromagnetische golven en straling. Technische Universiteit Eindhoven, Faculteit Elektrotechniek.

[18] J.M. Johnson and Y. Rahmat-Samii. Gentic algortihms in enineering electromagnetics. *IEEE Antennas and Propagation Magazine*, 39:7–21, 1997.

[19] N.A.A. Op den Kamp. Analysis and design of intravascular MR antennas. Master's thesis, Technische Universiteit Eindhoven, Faculteit Elektrotechniek, 2003.

[20] M.K. Konings, L.W. Bartels, H.F. Smits, and C.J. Bakker. Heating around intravascular guidewires by resonating RF waves. *Journal of Magnetic Resonance Imaging*, 12:79–85, 2000.

[21] T. Kuehne, R. Fahrig, and K. Butts. Pair of resonant fiducial markers for localization of endovascular catheters at all catheter orientations. *Journal of Magnetic Resonance Imaging*, 12:620–624, 2003.

[22] M.E. Ladd and H.H. Quick. Reduction of resonant RF heating in intravascular catheters using coaxial chockes. *Magnetic Resonance Imaging*, 12:534–546, 2000.

[23] M.E. Ladd, H.H. Quick, and J.F. Debatin. Interventional MRA and intervascular imaging. *Journal of Magnetic Rosonance Imaging*, 12:534–546, 2000.

[24] J.H. Letcher. Computer-assited design of surface coils used in magnetic resonance imaging I. the calculation of the magnetic field. *Magnetic Resonance Imaging*, 7:581–583, 1989.

[25] O. Ocali and E. Atalar. Intravascular magnetic resonance imaging using a loopless catheter antenna. *Magnetic Resonance in Medicine*, 37:112–118, 1997.

[26] U.S. Department of health and human services, Food and Drug Administration, Center for Devices and Radiological Health, CDRH Magnetic Resonance Working Group. A primer on medical device interactions with magnetic resonance imaging systems, 1997.

[27] PHILIPS. *Basic Principles of MR Imaging*. Philips Medical Systems, Best, The Netherlands.

[28] S. Ramo, J.R. Whinnery, and T. van Duzer. *Fields and Waves in Communication Electronics*. John Wiley & Sons, 1984.

[29] R.E.Collin. *Field Theory of Guided Waves,*. Mc Graw-Hill,, New York, 1960.

[30] E.W. Risely, Jr. Discontinuity capacitance of a coaxial line terminaed in a circular waveguide. *IEEE Transactions on Microwave Theory and Techniques*, MTT-17(2):86–92, 1969.

[31] M.N.O. Sadiku. *Elements of Electromagnetics*. Oxford University Press, New York, second edition, 1995.

[32] T. Schaeffter. Rs: Catheter tracking methods, mr - software / t5x6. PHILIPS, internal document, 2001.

[33] M.M. Weiner, S.P. Cruze, C.C. Li, and W.J. Wilson. *Monopole on Circular Ground Planes*. Artech House, 1987.

[34] S. Weiss. Active tracking catheter hardware, mr - software / t5x6. PHILIPS, internal document, 2001.

[35] S. Weiss, T. Kuehne, and M. Zenge. Switchable resonant fiducial marker for safe instrument localisation at all marker orientations. In *Proceedings of the ISMRM 10th Scientific Meeting and Exhibition*, page 2245, 2002.

[36] H. Whiteside and R.W.P. King. The loop antenna as probe. *IEEE Transactions on Antennas and Propagation*, 12:291–297, 1964.

[37] E.A. Wolff. *Antenna Analysis*. Artech House, 1988.

[38] E.Y. Wong, Q. Zhang, J.L. Duerk, J.S. Lewin, and M. Wendt. An optical system for wireless detuning of parallel resonant circuits. *Journal of Magnetic Resonance Imaging*, 12:632–638, 2000.

[39] D.A. Wrad and J. La T. Exo. Using rogowski coils for transient current measurements. *IEE Engineering and Science Journal*, pages 105–113, 1993.

[40] Q. Zhang, M. Wendt, A.J. Aschoff, J.S. Lewin, and J.L. Duerk. A multielement RF coil for MRI guidance of interventional devices. *Journal of Magnetic Resonance Imaging*, 14:56–62, 2001.

[41] Q. Zhang, M. Wendt, A.J. Aschoff, L. Zheng, J.S. Lewin, and J.L. Duerk. Active MR guidance of interventional devices with traget-navigation. *Magnetic Resonance in Medicine*, 44:56–65, 2000.

Appendix A

B field calculation

Part of the program code of the used FORTRAN routine for the calculation of the B field [24].

```
RK    = 0.1D-7
FOUR  = 4.0D0
TWO   = 2.0D0

DX01  = X0-X1
DY01  = Y0-Y1
DZ01  = Z0-Z1
DX21  = X2-X1
DY21  = Y2-Y1
DZ21  = Z2-Z1

A     = (DX01**2)+(DY01**2)+(DZ01**2)
B     = (-TWO)*(DX01*DX21+DY01*DY21+DZ01*DZ21)
C     = DX21**2+DY21**2+DZ21**2

DBX   = DY21*DZ01-DY01*DZ21
DBY   = DX01*DZ21-DX21*DZ01
DBZ   = DX21*DY01-DX01*DY21

WD    = (FOUR*A*C*DSQRT(A+B+C)-(B**2)*DSQRT(A+B+C))*
&         (FOUR*C*A**(1.5D0)-DSQRT(A)*B**2)
WN    = (-TWO*B*DSQRT(A+B+C)*(FOUR*A*C-B**2)+(TWO*B+FOUR*C)*
&         (FOUR*C*A**(1.5D0)-DSQRT(A)*(B**2)))

T     = RK*WN/WD

BX    = DBX*T
BY    = DBY*T
BZ    = DBZ*T
```

Part of the program code of the used FORTRAN routine for the rotation matrix [19].

```
CPH = COS(PHI)
SPH = SIN(PHI)
CPS = COS(PSI)
SPS = SIN(PSI)
CTH = COS(THETA)
STH = SIN(THETA)

RXX = CTH*CPS
RXY = CPS*STH
RXZ = -SPS

RYX = -CPH*STH+CTH*SPH*SPS
RYY = CTH*CPH+STH*SPH*SPS
RYZ = CPS*SPH

RZX = STH*SPH+CTH*CPH*SPS
RZY = -CTH*SPH+CPH*STH*SPS
RZZ = CPH*CPS

DO i=1,Nsegs*Nturns1

XC(i) = XA(i)*RXX + YA(i)*RXY + ZA(i)*RXZ
YC(i) = XA(i)*RYX + YA(i)*RYY + ZA(i)*RYZ
ZC(i) = XA(i)*RZX + YA(i)*RZY + ZA(i)*RZZ

END DO

DO i=1,Nsegs*Nturns2

XD(i) = XB(i)*RXX + YB(i)*RXY + ZB(i)*RXZ
YD(i) = XB(i)*RYX + YB(i)*RYY + ZB(i)*RYZ
ZD(i) = XB(i)*RZX + YB(i)*RZY + ZB(i)*RZZ

END DO

XA = XC
XB = XD
YA = YC
YB = YD
ZA = ZC
ZB = ZD
```

Appendix B

Induced EMF method

Consider a dipole antenna with current distribution

$$I(z) = I_m g(z) \tag{B.1}$$

where $g(z)$ is real. First we find potential $\mathbf{A}$ which has only a z component,

$$A_z = \int_{-l}^{l} \frac{\mu I_z e^{-jkR}}{4\pi R} dz' = \mu I_m \int_{-l}^{l} \frac{g(z')e^{-jk|z-z'|}}{|z-z'|} dz' \tag{B.2}$$

The electric field is given in terms of $\mathbf{A}$ by

$$\mathbf{E} = -j\omega \left[\mathbf{A} + \frac{1}{k^2} \nabla (\nabla \cdot \mathbf{A}) \right] = -j\omega \hat{\mathbf{z}} \left[A_z + \frac{1}{k^2} \frac{\partial^2 A_z}{\partial z^2} \right] \tag{B.3}$$

The portion of $\mathbf{E}$ in phase with the current causes the radiated power that clearly comes from the imaginary part of A_z. The integration of $I(z)E_{in-phase}$ over the antenna gives the total power transferred or radiated. This may be expressed in term of a radiation resistance

$$W = \int_{-l}^{l} I(z)(E_z)_{in-phase} dz = \frac{I_m^2 R_r}{2} \tag{B.4}$$

Substituting equations (B.2) and (B.3) in equation results in (B.4)

$$R_r = \frac{2\omega\mu}{4\pi} \int_{-l}^{l} dz \, g(z) \int_{-l}^{l} g(z') \left\{ \left[\frac{\sin k|z - z'|}{|z - z'|} \right] + \frac{\partial^2}{\partial z^2} \left[\frac{\sin k|z - z'|}{|z - z'|} \right] \right\} dz' \tag{B.5}$$

In evaluating these integral, series expansions of the $\sin k|z - z'|$ terms are often made. This method of finding radiation resistances of antennas is called the induced EMF method.

Appendix C

Calculation of C_{step}

The shunt capacitance C_{step}, see figure 4.13, is caused by the step in two coaxial cables with a different inner and/or outer conductor diameter and is given by [16, 15],

$$C_{step} = j \frac{2\pi\omega\mu_0\varepsilon_0\varepsilon_{r1}}{\ln(\frac{b_1}{a_1})} \left\{ \frac{\frac{y_{11}}{\gamma_{11}^2} < E_\rho, \Phi_{11} >^2 + \frac{y_{21}}{\gamma_{21}^2} < E_\rho, \Phi_{21} >^2}{< E_\rho, \Phi_0 >^2} \right.$$
$$\left. + \frac{\Sigma_{n=2}^{\infty} \frac{y_{1n}}{\gamma_{1n}^2} < E_\rho, \Phi_{1n} >^2 + \Sigma_{n=2}^{\infty} \frac{y_{2n}}{\gamma_{2n}^2} < E_\rho, \Phi_{2n} >^2}{< E_\rho, \Phi_0 >^2} \right\} \quad \text{(C.1)}$$

where ε_{r1} the relative permittivity of region 1, $\varepsilon_{r1} = 1$. y_{1n} and y_{2n} are the n-th TM mode admittances in regions 1 and 2 respectively. Gogioso et al. described the coaxial discontinuity through an equivalent transverse capacitance which takes into account the effects of the TM modes arising at both sides of the discontinuity. In order to calculate such capacitance, Gogioso et al. developed a variational following the general method given by Collin [29].

γ_{1n} and γ_{2n} are n-th the TM mode propagation constants [28],

$$y_{i,\,n} = \frac{1}{\eta}\sqrt{\frac{\omega^2}{\omega^2 - \omega_c^2}} \quad \text{(C.2)}$$

with

$$\omega_c = \frac{n\pi}{a_i\sqrt{\mu\varepsilon}} \quad \text{(C.3)}$$

$$\gamma_{i,\,n} = \sqrt{\left(\frac{n\pi}{a_i}\right)^2 - \omega^2\mu\varepsilon} \quad \text{(C.4)}$$

where i is the number of the used region and n is the number of the corresponding mode. η is defined by equation (4.4).

Φ_{1n} and Φ_{2n} are the corresponding n-th TM mode functions of the left and right region. Φ_0 is the TEM mode function in region 1 [12],

$$\Phi_0 = \frac{\ln(\rho/a_1)}{\sqrt{2\pi\ln(b_1/a_1)}} \quad \text{(C.5)}$$

Φ_{1n} and Φ_{2n} can be found by solving the scalar Helmholtz equation [17],

$$\nabla_t^2 + k_{t;n}^2 \Phi_n = 0 \qquad (C.6)$$

where $k_{t;n}$ is the propagation constant. Φ_{1n} and Φ_{2n} are now represented by Φ_n for simplicity. Equation (C.6) has to satisfy the boundary condition,

$$\Phi_n\big|_{\underline{\rho}=\underline{\rho}_\Gamma} = 0 \qquad (C.7)$$

where ρ is the radius and ρ_Γ is the the radius of the boundary. Thus, Φ_n has to be zero at the boundaries of the line. The boundary conditions for a coaxial cable are:

$$\Phi_{n;a} = \Phi_n\big|_{\rho_\Gamma=a_n} = 0 \qquad (C.8a)$$

$$\Phi_{n;b} = \Phi_n\big|_{\rho_\Gamma=b_n} = 0 \qquad (C.8b)$$

where a and b are the radii of the inner and outer conductor, respectively, figure 4.12. Φ_n is independent of the z-direction, so equation (C.6) can be written, in cylindrical coordinates, as,

$$\frac{\partial^2 \Phi_n}{\partial r^2} + \frac{1}{\rho}\frac{\partial \Phi_n}{\partial \rho} = -k_{t;n}^2 \Phi_n \qquad (C.9)$$

A solution to equation (C.9) is:

$$\Phi_n = C_1 J_0(k_{t;n}\rho) + C_2 Y_0(k_{t;n}\rho) \qquad (C.10)$$

where J_0 and Y_0 are the Bessel function of the first kind of order zero and the Bessel function of the second kind of order zero, respectively. To get a solution for Φ_n, the constants C_1, C_2 and $k_{t;n}$ have to be determined. This can be done by applying the boundary conditions of equation (C.8a,b) on equation (C.10),

$$C_1 J_0(k_{t;n}a) + C_2 Y_0(k_{t;n}a) = 0 \qquad (C.11a)$$

$$C_1 J_0(k_{t;n}b) + C_2 Y_0(k_{t;n}b) = 0 \qquad (C.11b)$$

Equation (C.10), equations (C.11a) and (C.11b) are combined into,

$$\begin{pmatrix} C_1 \\ C_2 \end{pmatrix} \cdot \begin{pmatrix} J_0(k_{t;n}a) & Y_0(k_{t;n}a) \\ J_0(k_{t;n}b) & Y_0(k_{t;n}b) \end{pmatrix} = \underline{0} \qquad (C.12)$$

which will yield zero when the determinant of the 2 × 2is zero, or,

$$J_0(k_{t;n}a)Y_0(k_{t;n}b) - J_0(k_{t;n}b)Y_0(k_{t;n}a) = 0 \qquad (C.13)$$

From equation (C.13) $k_{t;n}$ can be solved. This solution has to be substituted in equation (C.12) to get a solution for C_1 and C_2. $k_{t;n}$, C_1 and C_2 finally have to be substituted in equation (C.10) to obtain an expression for Φ_n.

In equation (C.1) is E_ρ the radial component of the electric field at the discontinuity and is approximated by [16],

$$E_\rho = e_0 \Phi_0 + e_1 \Phi_{11} \qquad (C.14)$$

77

where Φ_{11} is first TM mode functions of the left region. The coefficients e_0 and e_1 have values between zero and one.

The brackets, $< >$, in equation (C.1) denote the inner products over the region between the inner and outer conductors.

$y_{i,\ n}$, $\gamma_{i,\ n}$, Φ_n and E_ρ have to be substituted in equation (C.1),

$$
C_{step} = j \frac{2\pi\omega\mu_0\varepsilon_0\varepsilon_{r1}}{\ln(\frac{b_1}{a_1})} \left\{ \frac{\frac{y_{11}}{\gamma_{11}^2} < (e_0\Phi_0 + e_1\Phi_{11}), \Phi_{11} >^2 + \frac{y_{21}}{\gamma_{21}^2} < (e_0\Phi_0 + e_1\Phi_{11}), \Phi_{21} >^2}{< (e_0\Phi_0 + e_1\Phi_{11}), \Phi_0 >^2} \right.
$$
$$
\left. + \frac{\Sigma_{n=2}^{\infty}\frac{y_{1n}}{\gamma_{1n}^2} < (e_0\Phi_0 + e_1\Phi_{11}), \Phi_{1n} >^2 + \Sigma_{n=2}^{\infty}\frac{y_{2n}}{\gamma_{2n}^2} < (e_0\Phi_0 + e_1\Phi_{11}), \Phi_{2n} >^2}{< (e_0\Phi_0 + e_1\Phi_{11}), \Phi_0 >^2} \right\} \quad (C.15)
$$

To get the approximate value of the shunt capacitance C_{step}, equation (C.15) has to be minimised with respect to the coefficients e_0 and e_1 [15].